The Impact of the Ambient Gas Density on the Evolution of Supernova Remnants

by

Santiago Jiménez Villarraga

Thesis submitted in partial fullfillment of the requirements for the degree of

MASTER OF SCIENCE IN ASTROPHYSICS

at the

Instituto Nacional de Astrofísica, Óptica y Electrónica

November 2018

Tonantzintla, Puebla

Advised by:

PhD. Guillermo Tenorio-Tagle
Tenured Researcher INAOE
PhD. Sergiy Silich
Tenured Researcher INAOE

Abstract

This thesis presents a theoretical discussion of the full evolution of Supernova Remnants (SNRs), that includes the thermalization of the SN ejecta, the Sedov-Taylor and Snowplough stages of the SNR evolution. Our aim is to study how such evolution proceeds for different values of the ambient gas density. A fast numerical method based on the Thin-Shell approximation is developed.

The ejecta density and velocity configurations are included in order to study the ejecta-dominated (ED) or thermalization phase, and the transition to the Sedov-Taylor (ST) stage. The numerical scheme also includes radiative cooling. The calculations show that for low-density models, the remnants follow the classical evolutionary tracks with a negligible amount of energy radiated from the shocked ejecta gas and are in excellent agreement with the literature.

For high-density models, strong radiative cooling, both from the shocked ejecta and shocked ambient gas, leads the SNRs to evolve without reaching the ST stage. A critical ambient gas density is obtained. For densities higher than this critical value, the evolution differs significantly from the standard theory. In such cases, the remnants become radiative when the thermalization of the ejecta mass has not been concluded. Thus, the ambient density is an essential parameter on the evolution of SNRs.

Acknowledgment

This thesis has been possible thanks to an scholarship granted by CONACYT-México (registration number 613136). Additional support was provided by the Sistema Nacional de Investigadores (SNI), through its program of research assistants (grant number 620/2018) and from the Instituto Nacional de Astrofísica, Óptica y Electrónica (INAOE). I am profoundly grateful with Mexico and its people. I am also very grateful with my advisors, Dr. Guillermo Tenorio-Tagle and Dr. Sergiy Silich, for their guidance and constant support that made possible this thesis project. I would like to thank to all my professors, friends and staff of INAOE that helped me in countless occasions.

Contents

List of Figures

List of Tables

Chapter 1
Introduction

The explosions of massive stars at the end of their evolution (Supernova Explosions) are powerful sources of mass and energy. They shape the interstellar medium (ISM) of their host galaxies, determine the ISM chemical composition, compress the interstellar gas into fast moving shells and are sources of cosmic rays and of radio and X-ray emission (e.g McKee & Ostriker 1977, Terlevich et al. 1992, Tenorio-Tagle et al. 2015, Elmegreen 2017, Conroy & Spergel 2011, Silich & Tenorio-Tagle 2017, Krause et al. 2013). The SNRs are also dust producers in the Universe. The dust grains are assumed to form within the cold ejecta, such that the low temperatures and chemical composition of this gas permits the formation of dust grains (e.g Morgan et al. 2003, Nozawa et al. 2010, Todini & Ferrara 2001, Micelotta et al. 2016, Bianchi & Schneider 2007a).

The Supernova Remnants (SNRs), which formed when gas ejected by massive stars begins to interact with the ambient medium, undergo several stages (Chevalier, 1977).

The first stage, known as the **ejecta-dominated (ED) or thermalization phase**, begins when the high velocity expanding ejecta forms a leading shock in the ambient medium. The large thermal pressure behind this shock leads to the formation of another, reverse shock, which decelerates and thermalizes the ejected matter. At this stage, the velocity and density structure of the ejecta determines the dynamics of the SNRs (e.g Tang & Chevalier 2017, Draine & McKee 1993, McKee & Truelove 1995).

Cassiopeia A (Cas A) is an example of a SNR at this stage. It is a young ($\sim$ 400

yr old) SNR whose reverse shock still does not reach the center of the explosion. This implies that the thermalization of the ejected matter is still not completed in this case (e.g Micelotta et al. 2016, Laming & Hwang 2003,Laming & Hwang 2003, Orlando et al. 2016, Hwang & Laming 2012). Fig. 1.1 presents an image of CasA obtained with data from the Chandra X-ray Observatory.

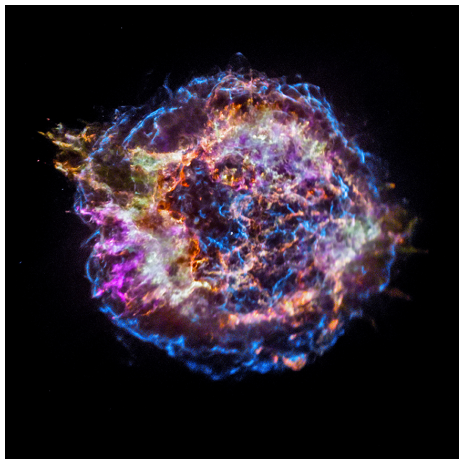

Figure 1.1: *Image of the Cas A SNR obtained by the Chandra Space Observatory. Image Credits: Nasa.*

After the thermalization process is terminated (i.e. when the reverse shock reaches the center of the explosion), the adiabatic **Sedov-Taylor (ST) solution** begins (e.g Sedov 1946, Bisnovatyi-Kogan & Silich 1995, Ostriker & McKee 1988). This stage is described by a self-similar hydrodynamic solution. This allows one to use the ST stage as a perfect test to verify new analytic and numerical methods designed to follow the evolution of SNRs. Indeed, during the ST stage, the shock radius and velocity are given by power-law functions of time ($R \propto t^{2/5}$, $V \propto t^{-3/5}$) and the kinetic and thermal energies are conserved ($E_k \approx 0.3E_0$ and $E_{th} \approx 0.7E_0$, where E_0 is the explosion energy, see Sedov 1946).

As the leading shock slows down with time, the post-shock temperature decreases ($T \propto V^2$) and reaches values which are close to the maximum in the cooling function

(e.g Raymond et al. 1976, Wiersma et al. 2009, Schure et al. 2009). Therefore, at late times radiative cooling becomes important. When this occurs, the remnant enters the **snowplough (SP)** phase (e.g Draine & McKee 1993, Cioffi et al. 1988a, Blondin et al. 1998, Mihalas & Mihalas 2013). At this stage, a very thin, cold and dense shell is formed at the outer boundary of the SNR. The density increases in response to the sudden fall of post-shock temperature, due to radiative cooling, to preserve pressure.

Throughout the course of the SP stage, a SNR loses most of its thermal energy. The remnant then moves for a while in the **momentum conserving conservation stage (MCS)** and finally merges with the ambient gas when the expansion velocity drops to the sound speed in the ambient ISM .

The evolutionary tracks described above were successfully applied to many SNRs (e.g Orlando et al. 2016, McKee & Ostriker 1977, Borkowski et al. 2001, Slane et al. 2000). However, they do not explain the evolution of all the SNRs. The major factors which the standard theory does not consider are the non-homogeneity of the ambient medium and the radiative loses of energy at the early ED-phase in cases when the SN explosion occurs in a high density ambient medium. For example, Terlevich et al. (1992) found that when the ambient gas density is $n_0 = 10^7$ cm^{-3}, strong radiative cooling speeds up the evolution and the SNR does not reach the ST stage.

Thus, the ambient density is an important parameter that must be considered in order to understand the evolution of SNRs and their feedback on their host galaxies. However, the numerical simulation of SN explosions at such high densities are computationally expensive, as small time steps are required in order to take into account the radiation terms properly (LeVeque et al., 2006).

The aim of this Thesis

The evolution of SNRs dramatically differs when the explosion occurs in low and high density media. However, given the difficulty of numerical simulations for large ambient densities n_0, the evolution of SNRs in these cases is not well understood. This problem is addressed in this thesis. Our aim is to develop a numerical code

that allows one to follow the evolution of SNRs from the ejecta-dominated phase to the Snowplough stage for any ambient gas density. In order to achieve this aim, we included all necessary terms in the Thin-Shell approximation equations to take into account the ejecta density and velocity structure and the effects of radiative cooling at all possible ambient densities.

Structure of the Thesis

- The basic Thin-Shell approximation (TSA) and its implementation as a 3D numerical code is discussed in **chapter 2**. The method is tested by reproducing the Sedov-Taylor results. Additionally, a test of a SNR evolving into a non-homogeneous ambient medium is shown.

- The TSA is extended to cover the thermalization of the ejecta mass in **chapter 3**. To achieve this, the ejecta density and free expansion velocity are introduced. The reverse shock dynamics is also included. The method relies on the energy conservation equation in order to follow this evolutionary phase. Our results for the dynamics of both the leading and the reverse shocks are discussed and compared with previous analytic and numerical results. The impact of the initial conditions of the ejected material on the long-term evolution of SNRs is also discussed.

- **Chapter 4** deals with the transition from the Sedov-Taylor stage to the Snowplough phase. Hence, the cooling function is presented and a radiation term for the leading shock is added to the TSA. The transition time between both stages is defined, calculated and compared with previous results. It is shown that during the ST stage, the leading shock moves approximately as $R \propto t^{0.39}$ and during the Snowplough stage as $R \propto t^{0.3}$.

- **Chapter 5** merges the previous chapters to study the full SNR evolution for different densities of the ambient medium. In order to achieve this, a radiation term for the shocked ejecta is also include in the TSA code. For low density models, the energy lost by the ejecta gas due to radiative cooling is shown to be negligible. The radiated energy from the leading shock is shown to peak about

the transition time to the Snowplough stage. Later, a study of the impact of the ambient medium on the thermalization of the ejecta mass for a wide range of densities is presented. The highest density that allows a SNR to thermalize its ejecta mass before reaching the SP stage, is determined. For higher densities, part of the ejecta mass still has not been shocked when the remnants become fully radiative.

- Finally, **chapter 6** summarizes the main results, presents the conclusions of this work and discusses briefly possible future directions.

Chapter 2

The Thin-Shell Approximation

Introduction

Supernova explosions produce an important feedback on the interstellar medium due to the injection of a huge amount of energy and momentum (e.g. Silich & Tenorio-Tagle 2017; McKee & Ostriker 1977; Conroy & Spergel 2011; Tenorio-Tagle et al. 2015). SNRs also play a pivotal role on the contamination of the surrounding medium with metal-rich gas generated both as by-products of the explosion and during the life of the star (Tenorio-Tagle, 1996).

Modelling the dynamical evolution of a supernova explosion in the ISM requires solving the hydrodynamic equations with sophisticated numerical tools and demands high spatial and temporal resolution making the solution computationally expensive (Mihalas & Mihalas, 2013; LeVeque et al., 2006). In many cases, however, a much simpler method known as the **the Thin-Shell Approximation (TSA)**, could be used to follow faithfully the 3D evolution of SNRs even in non-uniform media[1]. The theoretical foundation and numerical implementation of this method is discussed in this chapter. Although the focus will be on describing the adiabatic solution, subsequent chapters discuss a generalization of this method that allows one to follow the full evolution of SNRs from the ejecta dominated phase to the radiative phase.

[1]See a review by Bisnovatyi-Kogan & Silich (1995) and references therein.

Model equations

The Thin-Shell approximation was developed several decades ago and is based on two basic assumptions: the first one is that, gas swept-up by the shock is concentrated in a shell which is thin compared to the size of the remnant (e.g. Clarke & Carswell 2007, Mihalas & Mihalas 2013, Draine & McKee 1993) and it is moving with the shocked-gas velocity $\mathbf{U}$ (which for an adiabatic shock is just $U = \frac{2}{\gamma+1}V_s$, where V_s is the shock velocity and γ is the ratio of the specific heats). The second assumption is that the gas thermal pressure is uniform throughout the volume enclosed by the leading shock.

In non-spherical cases, the shell must be split in a set of N Lagrangian elements and one has to follow the motion of each of these elements by making use of the equations of mass and momentum conservation. The set of equations is coupled by means of the energy conservation equation.

Blast wave dynamics

Let us consider a single Lagrangian element with mass μ, velocity $\mathbf{U}$ and radius-vector $\mathbf{r}$. The equations of mass and momentum conservation can be written then as (Silich, 1992):

$$\frac{d\mu}{dt} = \frac{\gamma+1}{2}\rho\left(x,y,z\right)\left(\mathbf{U}-\mathbf{V}\right)\cdot\mathbf{n}d\Sigma \tag{2.2.1}$$

$$\frac{d}{dt}\left(\mu\mathbf{U}\right) = P\mathbf{n}d\Sigma + \mathbf{V}\frac{d\mu}{dt} + \mu\mathbf{g} \tag{2.2.2}$$

$$\frac{d\mathbf{r}}{dt} = \frac{\gamma+1}{2}\mathbf{U} \tag{2.2.3}$$

Where $\rho\left(x,y,z\right)$ and $\mathbf{V}\left(x,y,z\right)$ are the density and velocity of the unshocked, surrounding medium, $d\Sigma$ is the area of the Lagrangian element, $\mathbf{n}$ is the unit vector normal to the surface of the Lagrangian element, $\mathbf{g}$ is the gravitational acceleration and P is the thermal pressure inside the remnant, which is determined by the energy conservation equation.

As it is well known (e.g. Apostol 2007), any surface can be parametrized with two

parameters λ_1 and λ_2. The surface of any Lagrangian element $d\Sigma$ and the unit vector $\mathbf{n}$ are, respectively:

$$d\Sigma = S d\lambda_1 d\lambda_2, \tag{2.2.4}$$

$$\mathbf{n} = \frac{1}{S}\frac{\partial(y,z)}{\partial(\lambda_1,\lambda_2)}\hat{\mathbf{n}}_\mathbf{x} + \frac{1}{S}\frac{\partial(z,x)}{\partial(\lambda_1,\lambda_2)}\hat{\mathbf{n}}_\mathbf{y} + \frac{1}{S}\frac{\partial(x,y)}{\partial(\lambda_1,\lambda_2)}\hat{\mathbf{n}}_\mathbf{z}, \tag{2.2.5}$$

where:

$$S = \sqrt{\left(\frac{\partial(y,z)}{\partial(\lambda_1,\lambda_2)}\right)^2 + \left(\frac{\partial(z,x)}{\partial(\lambda_1,\lambda_2)}\right)^2 + \left(\frac{\partial(x,y)}{\partial(\lambda_1,\lambda_2)}\right)^2} \tag{2.2.6}$$

and $\partial(x_i,x_j)/\partial(\lambda_i,\lambda_j)$ are the Jacobians. The volume enclosed by the surface is calculated as:

$$\Omega = \frac{1}{3}\int\int\left[x\frac{\partial(y,z)}{\partial(\lambda_1,\lambda_2)} + y\frac{\partial(z,x)}{\partial(\lambda_1,\lambda_2)} + z\frac{\partial(x,y)}{\partial(\lambda_1,\lambda_2)}\right]d\lambda_1 d\lambda_2 \tag{2.2.7}$$

Using equations 2.2.4, 2.2.5 and 2.2.6, one can write equations 2.2.1, 2.2.2 and 2.2.3 in cartesian coordinates as:

$$\frac{d\mu}{dt} = \frac{\gamma+1}{2}\rho\epsilon, \tag{2.2.8}$$

$$\frac{dU_x}{dt} = \frac{P}{\mu}\frac{\partial(y,z)}{\partial(\lambda_1,\lambda_2)} - \frac{U_x - V_x}{\mu}\frac{d\mu}{dt} + g_x, \tag{2.2.9}$$

$$\frac{dU_y}{dt} = \frac{P}{\mu}\frac{\partial(z,x)}{\partial(\lambda_1,\lambda_2)} - \frac{U_y - V_y}{\mu}\frac{d\mu}{dt} + g_y, \tag{2.2.10}$$

$$\frac{dU_z}{dt} = \frac{P}{\mu}\frac{\partial(x,y)}{\partial(\lambda_1,\lambda_2)} - \frac{U_z - V_z}{\mu}\frac{d\mu}{dt} + g_z, \tag{2.2.11}$$

$$\frac{dx}{dt} = \frac{\gamma+1}{2}U_x, \quad \frac{dy}{dt} = \frac{\gamma+1}{2}U_y, \quad \frac{dz}{dt} = \frac{\gamma+1}{2}U_z, \tag{2.2.12}$$

where x, y, z, U_x, U_y, U_z are the cartesian coordinates of the position and velocity vectors of the Lagrangian element and:

$$\epsilon = (U_x - V_x)\frac{\partial(y,z)}{\partial(\lambda_1,\lambda_2)} + (U_y - V_y)\frac{\partial(z,x)}{\partial(\lambda_1,\lambda_2)}(U_z - V_z)\frac{\partial(x,y)}{\partial(\lambda_1,\lambda_2)}. \tag{2.2.13}$$

The gas thermal pressure P changes with time, but remains uniform inside the remnant and is equal to:

$$P = (\gamma - 1)\frac{E_{th}}{\Omega}. \tag{2.2.14}$$

In equation 2.2.14, Ω is the volume which is calculated using equation 2.2.7 and E_{th} is the SNR thermal energy:

$$E_{th} = E_0 - E_k, \tag{2.2.15}$$

where E_0 is the initial explosion energy and E_k is the kinetic energy:

$$E_k = \frac{1}{2}\int\int \mu U^2 d\lambda_1 d\lambda_2. \tag{2.2.16}$$

In order to solve equations (2.2.8-2.2.12) numerically, it is necessary to compute the determinants $\partial(x_i, x_j)/\partial(\lambda_i, \lambda_j)$ and formulate the initial conditions for each Lagrangian element.

Numerical Method: Code description

Computing the Jacobian Determinants

Let us split the remnant into a set of Lagrangian elements with indexes (i, j), where $i \in \{1, \ldots, N_z\}$ and $j \in \{1, \ldots, N_\phi\}$. The Jacobian for a given Lagrangian element is:

$$\frac{\partial(x, y)}{\partial(\lambda_1, \lambda_2)} = \begin{vmatrix} \frac{\partial x}{\partial \lambda_1} & \frac{\partial x}{\partial \lambda_2} \\ \frac{\partial y}{\partial \lambda_1} & \frac{\partial y}{\partial \lambda_2} \end{vmatrix} = \frac{\partial x}{\partial \lambda_1}\frac{\partial y}{\partial \lambda_2} - \frac{\partial x}{\partial \lambda_2}\frac{\partial y}{\partial \lambda_1}. \tag{2.3.1}$$

To calculate 2.3.1 for the element (i, j), its closest neighbours are used. In other words, the derivatives on the point (i, j) are calculated as finite differences with respect to the surrounding points. Hence:

$$\frac{\partial x(i, j)}{\partial \lambda_1} = \frac{x(i+1, j) - x(i-1, j)}{d\lambda_1}, \tag{2.3.2}$$

$$\frac{\partial x(i, j)}{\partial \lambda_2} = \frac{x(i, j+1) - x(i, j-1)}{d\lambda_2}, \tag{2.3.3}$$

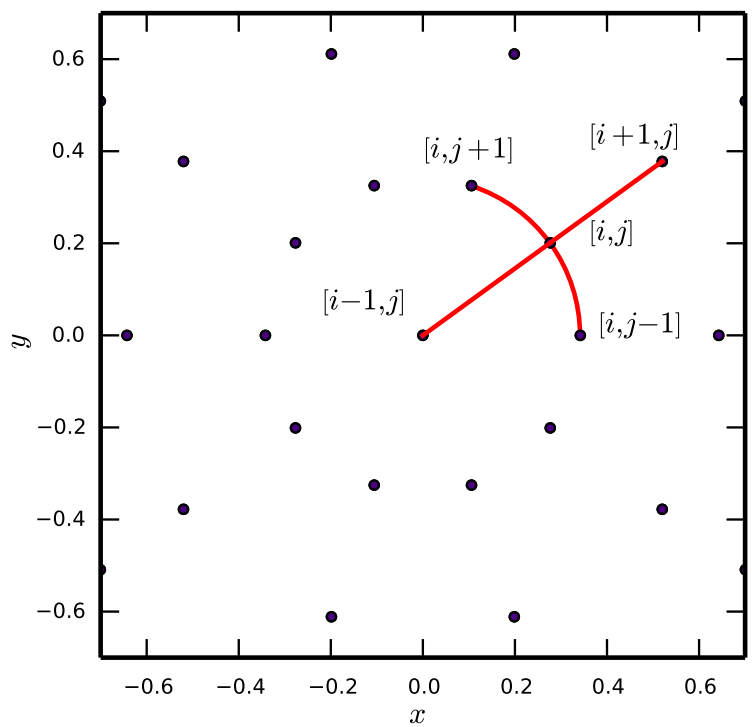

Figure 2.1: *Illustration of the procedure used to compute the Jacobian Matrices. Its is shown an arbitrary point. This plot is a projection of the sphere onto the xy plane.*

$$\frac{\partial y\,(i,j)}{\partial \lambda_1} = \frac{y\,(i+1,j) - y\,(i-1,j)}{d\lambda_1}, \tag{2.3.4}$$

$$\frac{\partial y\,(i,j)}{\partial \lambda_2} = \frac{y\,(i,j+1) - y\,(i,j-1)}{d\lambda_2}, \tag{2.3.5}$$

$$\frac{\partial z\,(i,j)}{\partial \lambda_1} = \frac{z\,(i+1,j) - z\,(i-1,j)}{d\lambda_1}, \tag{2.3.6}$$

$$\frac{\partial z\,(i,j)}{\partial \lambda_2} = \frac{z\,(i,j+1) - z\,(i,j-1)}{d\lambda_2}. \tag{2.3.7}$$

As the values of the coordinates at each Lagrangian point are known, it is possible to calculate the Jacobians 2.3.1 at each Lagrangian element. Fig. 2.1 illustrates this procedure. Here the red lines indicate the neighbour points used to calculate the

derivatives over the two variables.

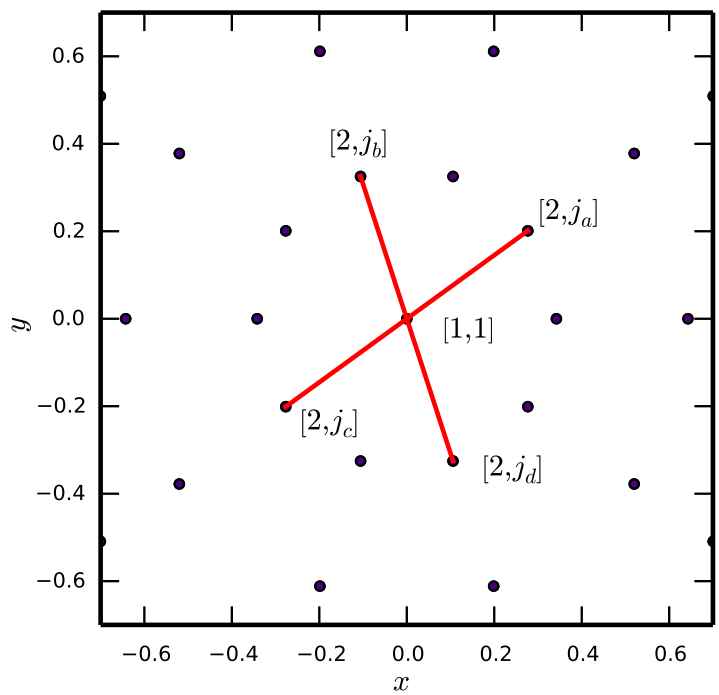

Figure 2.2: *Same as Fig. 2.1 but for the north pole.*

In order to compute the Jacobians for the poles, one should select points which belong to the first Lagrangian layer above or bellow the pole. Introducing the following notation:

$$j_a = 1 \tag{2.3.8}$$

$$j_b = \frac{N_\phi}{4} + 1 \tag{2.3.9}$$

$$j_c = \frac{N_\phi}{2} + 1 \tag{2.3.10}$$

$$j_d = \frac{3N_\phi}{4} + 1 \tag{2.3.11}$$

For clarity, Fig. 2.2 shows these points for the north pole. In this case the derivatives are calculated as:

$$\frac{\partial x\left(1,1\right)}{\partial \lambda_1} = \frac{x\left(2,j_c\right) - x\left(2,j_a\right)}{d\lambda_1}, \tag{2.3.12}$$

$$\frac{\partial x\left(1,1\right)}{\partial \lambda_2} = \frac{x\left(2,j_d\right) - x\left(2,j_b\right)}{d\lambda_2}, \tag{2.3.13}$$

$$\frac{\partial y\left(1,1\right)}{\partial \lambda_1} = \frac{y\left(2,j_c\right) - y\left(2,j_a\right)}{d\lambda_1}, \tag{2.3.14}$$

$$\frac{\partial y\left(1,1\right)}{\partial \lambda_2} = \frac{y\left(2,j_d\right) - y\left(2,j_b\right)}{d\lambda_2}, \tag{2.3.15}$$

$$\frac{\partial z\left(1,1\right)}{\partial \lambda_1} = \frac{z\left(2,j_c\right) - z\left(2,j_a\right)}{d\lambda_1}, \tag{2.3.16}$$

$$\frac{\partial z\left(1,1\right)}{\partial \lambda_2} = \frac{z\left(2,j_d\right) - z\left(2,j_b\right)}{d\lambda_2}. \tag{2.3.17}$$

This allows one to compute the Jacobian determinants for every Lagrangian element. The accuracy of the calculations depends on the number of elements and becomes better if more Lagrangian zones are used (large N_z and N_ϕ). As an illustrative example, Fig. 2.3 shows the relative errors $\epsilon = \left(V_{real} - V_{comp}\right)/V_{real}$ of computing the volume V_{comp} of the initial sphere by means of equation 2.2.7. The standard case used for this work is: $N_z = N_\phi = 40$.

Setting the initial conditions

It is assumed that at $t = 0$ the remnant is spherical. It is split into a number of Lagrangian elements whose cartesian coordinates are determined by a user-selected set of points in the azimuth ($N_\phi$points) and polar (N_z points) directions. Let $\Delta\alpha_i$ and $\Delta\alpha_j$ be the angles that separate points in these directions:

$$\Delta\alpha_i = \frac{\pi}{Nz - 1}, \qquad \Delta\alpha_j = \frac{2\pi}{N_\phi} \tag{2.3.18}$$

Then, for every $i \in \{1, \ldots, N_z\}$ and for every $j \in \{1, \ldots, N_\phi\}$, the initial positions and velocities of the Lagrangian elements for a remnant of initial radius R_0 and velocity U_0, whose center is located at (x_0, y_0, z_0) are:

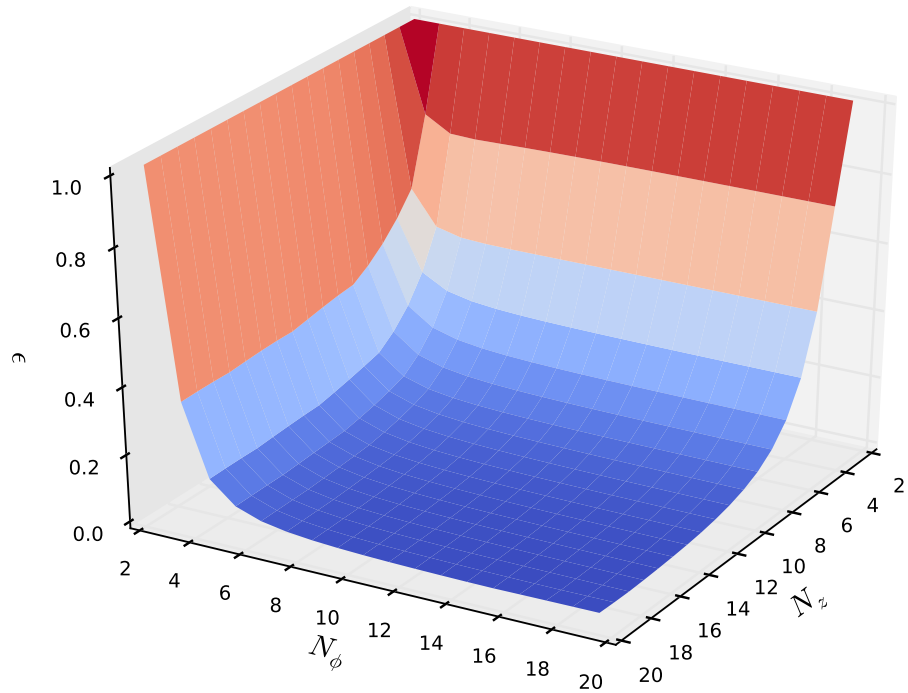

Figure 2.3: *Relative error* $\epsilon = (V_{real} - V_{comp})/V_{real}$ *of computing the volume of a sphere with equation 2.2.7.*

$$x_{ij} = R_0 \sin\alpha_i \cos\alpha_j + x_0, \tag{2.3.19}$$

$$y_{ij} = R_0 \sin\alpha_i \sin\alpha_j + y_0, \tag{2.3.20}$$

$$z_{ij} = R_0 \cos\alpha_i + z_0, \tag{2.3.21}$$

$$Vx_{ij} = U_0 \sin\alpha_i \cos\alpha_j, \tag{2.3.22}$$

$$Vy_{ij} = U_0 \sin\alpha_i \sin\alpha_j, \tag{2.3.23}$$

$$Vz_{ij} = U_0 \cos\alpha_i, \tag{2.3.24}$$

where:

$$\alpha_i = (i-1)\,\Delta\alpha_i, \quad \alpha_j = j\Delta\alpha_j. \tag{2.3.25}$$

Fig. 2.4 shows the initial positions for the Lagrangian elements in the case when the

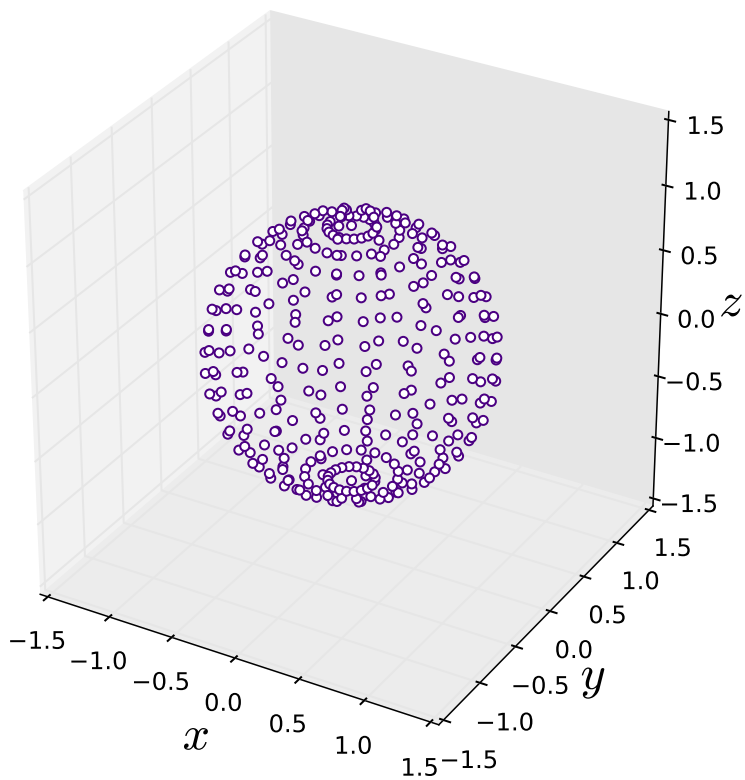

Figure 2.4: *Initial positions for the Lagrangian elements with* $N_z = N_\phi = 20$.

initial remnant radius is 1 pc and $N_z = N_\phi = 20$. These definitions determine how many ordinary differential equations (ODEs) must be solved per time step. The total number of Lagrangian elements in the simulation is:

$$N_{tot} = N_\phi \left(N_z - 2\right) + 2. \tag{2.3.26}$$

As every Lagrangian element is described by 7 ODE's (equations (2.2.8-2.2.12)), which must be combined with the global equation of energy conservation, the total number

of differential equations that must be solved every time step is:

$$N_{eq} = 7N_{tot} + 1 = 7\left(N_{\phi}\left(N_z - 2\right) + 2\right) + 1. \tag{2.3.27}$$

In a typical run of the code (i.e., $N_{\phi} = N_z = 40$), the total number of differential equations N_{eq} is 10655.

Dimensionless form of the main equations

The initial conditions are used to present the main equations in a dimensionless form. The initial radius R_0 and shell velocity U_0 are the length and velocity units, respectively, and the coordinates and velocities of the Lagrangian elements are normalized as:

$$x'_{i,j} = x_{i,j}/R_0, \quad y'_{i,j} = y_{i,j}/R_0, \quad z'_{i,j} = z_{i,j}/R_0, \tag{2.3.28}$$

$$Vx'_{i,j} = Vx_{i,j}/U_0, \quad Vy'_{i,j} = Vy_{i,j}/U_0, \quad Vz'_{i,j} = Vz_{i,j}/U_0. \tag{2.3.29}$$

The mass is measured in the units:

$$M_{unit} = \rho\left(x_0, y_0, z_0\right) R_0^3. \tag{2.3.30}$$

The initial swept up mass then is:

$$M' = \frac{M_0}{M_{unit}} = \frac{4\pi}{3}.$$

The initial total energy of the remnant E_0 is used as the unit of energy. Then the pressure is measured in the units:

$$P_{unit} = \frac{E_0}{R_0^3}. \tag{2.3.31}$$

Finally, the time scale is defined as:

$$t_{unit} = \frac{R_0}{U_0}. \tag{2.3.32}$$

To solve the set of dimensionless equations we adapted the Dormand-Prince method for the eight order Runge-Kutta-Fehlberg integrator (Dormand & Prince, 1980), coupled with a proportional-integral (PI) stepsize control (Press, 2007). This algorithm guaranties that the integration is performed under a user-selected value for the tolerance and it also calculates the value of the next time step h. This is done for every Lagrangian element, which implies that in order to keep the same time step for the entire remnant, one should select the minimum time step calculated for all Lagrangian elements as the new h for the following integration.

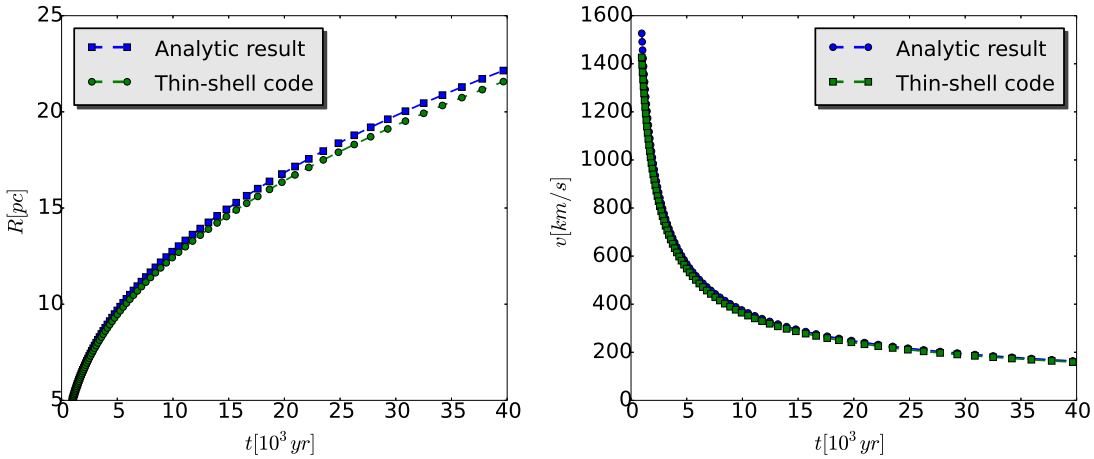

Figure 2.5: *Comparison of the numerical simulation with the Sedov-Taylor solution: the remnant radius and shock expansion velocity.*

Testing the code

In order to verify the numerical method described before, the evolution of a SNR in the uniform ISM is compared with the well known Sedov-Taylor (ST) solution.

Sedov-Taylor solution

As discussed in section 2.3.2, in order to start a calculation, it is necessary to fix the initial radius and velocity of the remnant. The ST- solution is a self-similar solution

in which the radii of the remnant is a power-law function of time (e.g. Zel'dovich & Raizer 2012; Bisnovatyi-Kogan & Silich 1995):

$$R = (\xi_0 E_0/\rho_0)^{1/5}\, t^{2/5}, \tag{2.4.1}$$

Where $\xi_0 = 2.026$, E_0 is the explosion energy and ρ_0 is the ISM density. The initial radius of the remnant is fixed, equation 2.4.1 then determines the initial time t_0 and the initial velocity of the remnant.

$$v_0 = \frac{dR}{dt}\Big|_{t=t_0} = \frac{2}{5}\frac{R_0}{t_0}, \tag{2.4.2}$$

Fig. 2.5 presents the results of the calculation in the case when the energy of the explosion is $E_0 = 10^{51}$ erg and the ISM number density is $n_0 = 1$ cm^{-3}, although results were obtained also for a wide range of values of the parameter space (n_0, E).

In the ST solution, the thermal and kinetic energies of the remnant are (Sedov, 1946):

$$E_{th} = \frac{\gamma+1}{3\gamma-1}E, \quad E_k = 2\frac{\gamma-1}{3\gamma-1}E \tag{2.4.3}$$

These energies are compared to those predicted by the Thin-Shell code.

In the case when the specific heats ratio is $\gamma = 5/3$: $E'_{th} = 2/3$ and $E'_k = 1/3$. Mass conservation is checked by comparing the swept-up mass with that located inside a sphere of radius $R = R_s$, where R_s is the shock radius.

Fig. 2.5 shows the comparison of the shock position and expansion velocity calculated by the Thin-Shell code with the ST solution. One can note that the numerical results are in very good agreement with equation 2.4.1. Fig. 2.6 shows the evolution of the kinetic and thermal energies. It is clear that the code conserves the total energy and predicts the proper fractions for the kinetic and thermal energies of the remnant.

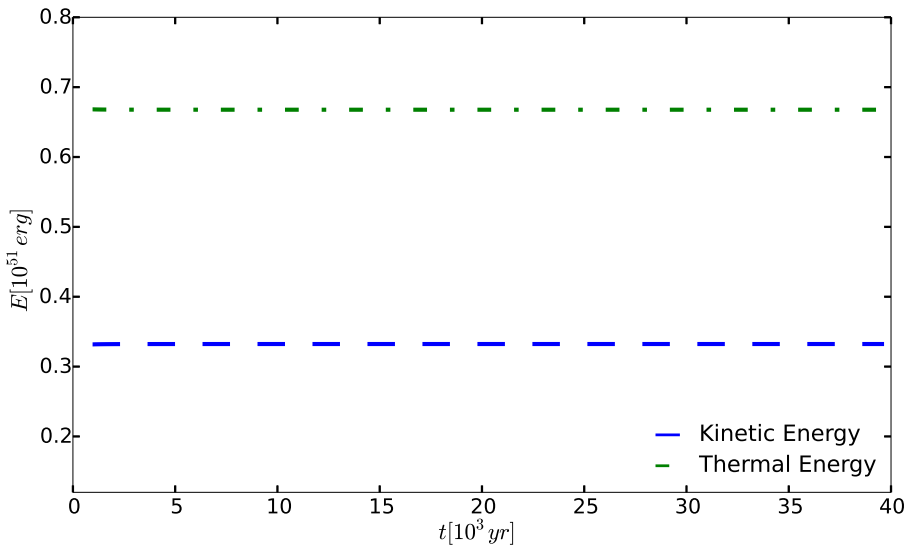

Figure 2.6: *Comparison of the numerical simulation with the Sedov-Taylor solution: Values of kinetic and thermal energies provided by the integration.*

Finally, Fig. 2.7 shows the swept-up mass compared to the mass that initially was contained in a sphere with radius R and density ρ_0. Fig. 2.7 proves that the code implemented in this work conserves mass very accurately.

SNRs expanding in an ellipsoidal density distribution

As it has been long known, most of the old supernova remnants are not spherical (Hnatyk & Petruk, 1999). Their morphologies reflect the basic property of shock waves of moving faster into regions of lower densities (e.g. Zel'dovich & Raizer 2012; Draine & McKee 1993). To test how the code reproduces the expansion of shock waves evolving into an inhomogeneous ISM, it was assumed an ellipsoidal ambient density distribution:

$$\rho = \rho_0 \left[\frac{1-\alpha_0}{1+(x/x_0)^2+(y/y_0)^2+(z/z_0)^2} + \alpha_0 \right], \tag{2.4.4}$$

where $\alpha_0 = 0.01$, $n_0 = \rho_0/\mu = 1$ cm^{-3}, $x_0 = 2$ pc, $y_0 = 4$ pc and $z_0 = 8$ pc. Fig. 2.8 shows the results of the calculations when the remnant age is $t \approx 9500$ yr whereas Fig. 2.9 shows the slices over the three planes. As expected, the symmetry is

lost, the remnant traces regions of low and high densities in excellent agreement with Bisnovatyi-Kogan & Silich (1995).

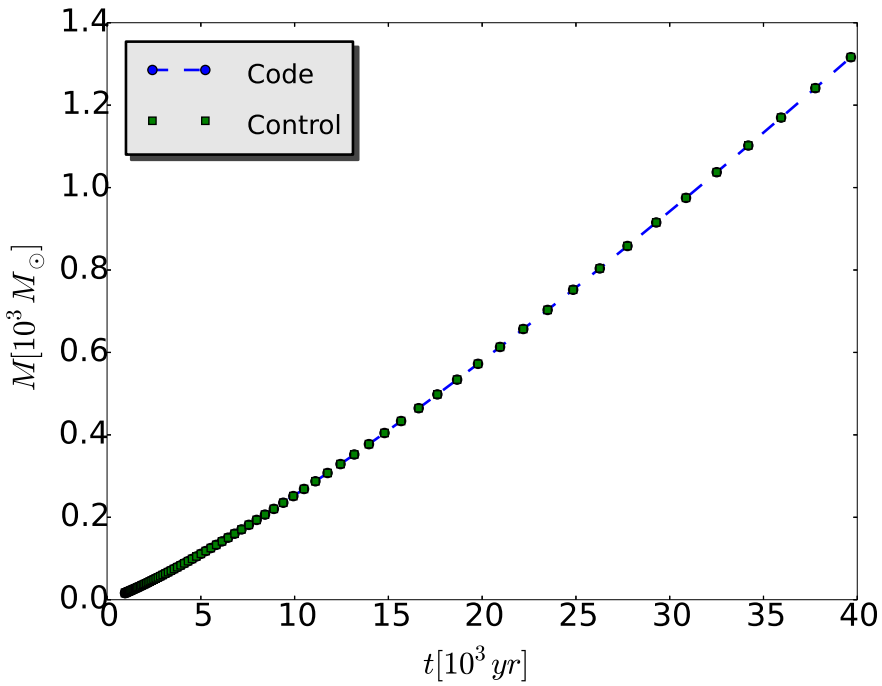

Figure 2.7: *Mass conservation: it is compared the mass swept-up by the Thin-Shell code, calculated by adding up the masses of every Lagrangian element, with the mass that initially was contained in a sphere of radius R in a medium of uniform density (which we call the control mass).*

Summary

This chapter has introduced the basic numerical scheme based on the Thin-Shell approximation. The main equations have been described together with the numerical method which allows one to follow the evolution of SNRs in an inhomogeneous media. The implemented code reproduced well the Sedov-Taylor analytic predictions for a homogeneous medium, including the shock radius, the expansion velocity, and also

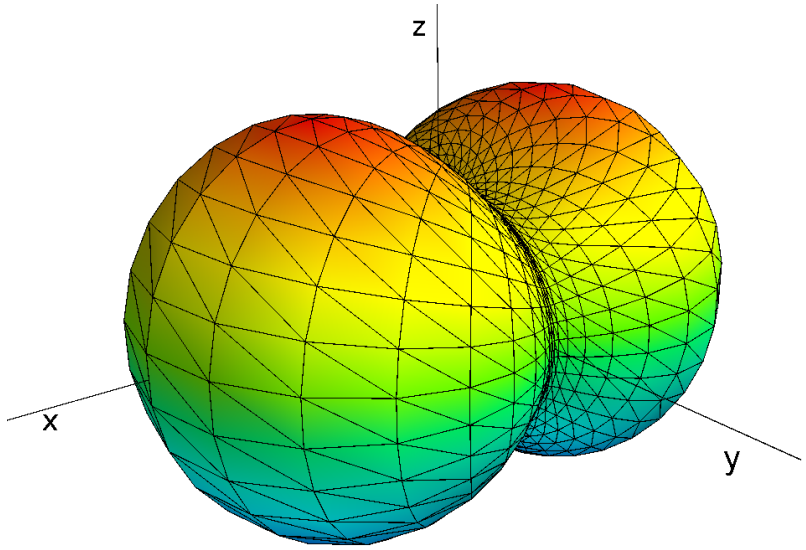

Figure 2.8: *3D Remnant generated by SNe into an ellipsoidal density distribution.*

the values of the thermal and kinetic energies. Cases with an inhomogeneous density medium were also considered and the results are in good agreement with the results in the literature. This code is the core for the remaining parts of this work and the following chapter discusses a method for extending this numerical scheme to cover also the initial phase of SNRs evolution, i.e., the ejecta-dominated phase.

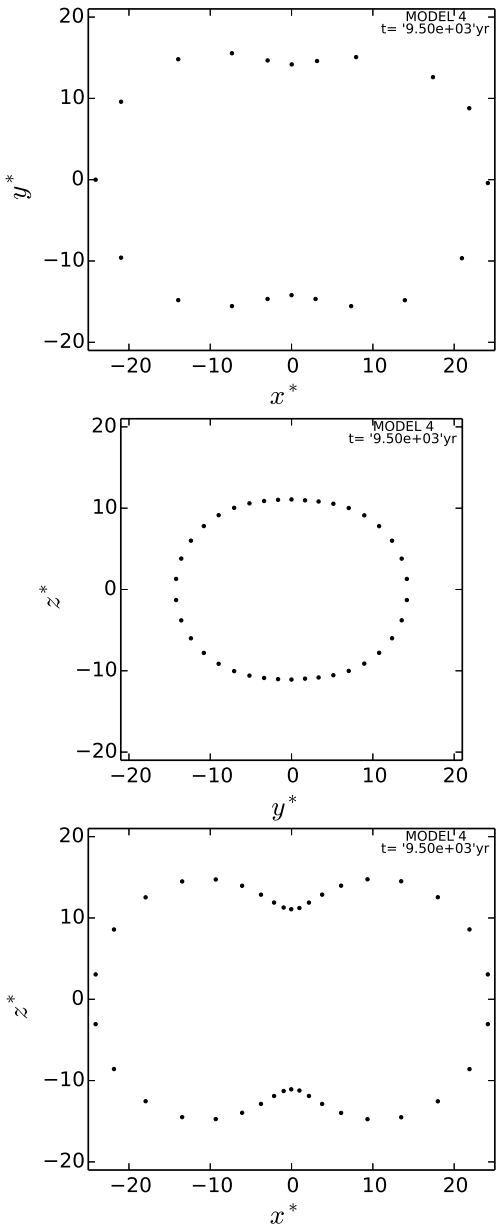

Figure 2.9: *Slices in the three planes for the remnant shown in Fig. 2.8.*

Chapter 3

The ejecta-dominated Phase

Introduction

There is an increasing observational data from young SNRs (Hwang & Laming 2012; Laming & Hwang 2003) that show features of a double-shock structure, implying that the freely expanding ejecta is still dynamically important for these remnants. Moreover, as demonstrated by Terlevich et al. 1992, the evolution of an SNR in a high density ambient medium could prevent totally the existence of the adiabatic ST-stage due to strong radiative cooling. Therefore, one cannot always start the study of SNR from the ST solution and a theoretical understanding of the ejecta-dominated (ED) phase (e.g, Micelotta et al. 2016; Orlando et al. 2016) is needed in order to study young SNRs or remnants evolving into a high density media.

This chapter presents an extension of the numerical scheme discussed in the previous chapter, that allows to simulate the evolution of SNRs from the ED-phase. The dynamics of the reverse shock, which moves into the ejected matter, is considered. This secondary shock is dynamically relevant as it thermalizes the rapidly expanding ejecta.

In the ED-phase, the ejecta mass and its density structure play a dominant role, so additional equations must be introduced to describe the dynamics of the reverse shock and the region between the leading and the reverse shocks. This introduces a new dimensional parameter: the ejecta mass M_{ej}. Nevertheless, the basic system of units introduced in the previous chapter is kept through this chapter.

The density and velocity structure of the ejecta

The ejecta is considered to have a negligible thermal pressure and to be freely expanding. Its velocity then is:

$$v\left(r,t\right)=\begin{cases}\frac{r}{t} & \text{if } r\leq R_{ej},\\ 0 & \text{if } r>R_{ej},\end{cases} \tag{3.2.1}$$

where $R_{ej}=v_{ej}t$. The distribution of density in the ejecta is assumed to be given by:

$$\rho_{ej}\left(r,t\right)=\frac{M_{ej}}{v_{ej}^{3}}f\left(\frac{v}{v_{ej}}\right)t^{-3}, \tag{3.2.2}$$

where M_{ej} and v_{ej} are the ejecta mass and the free-expansion velocity, respectively. $f\left(v/v_{ej}\right)$ is a function which determines the time-independent spatial structure of the ejecta. Power law functions are considered hereafter:

$$f\left(w\right)=\begin{cases}f_{0} & \text{if } 0\leq w\leq w_{core},\\ f_{n}w^{-n} & \text{if } w_{core}\leq w\leq 1,\end{cases} \tag{3.2.3}$$

where:

$$w=\frac{v}{v_{ej}},\qquad w_{core}=\frac{v_{core}}{v_{ej}}. \tag{3.2.4}$$

In this equation v_{core} is the velocity of the ejecta at the core radius and f_0 and f_n are parameters determined by continuity and mass normalization (Truelove & McKee, 1999, hereafter TM99). A core is required for obtaining a finite mass M_{ej} when the ejecta index $n>3$. Here it is assumed that $n<3$, and thus $v_{core}=0$. In such cases, the constant f_n is (TM99):

$$f_{n}=\frac{3-n}{4\pi},\qquad n<3, \tag{3.2.5}$$

and:

$$\frac{E_{0}}{\left(1/2\right)M_{ej}v_{ej}^{2}}=\alpha, \tag{3.2.6}$$

where:

$$\alpha=\frac{3-n}{5-n},\qquad n<3. \tag{3.2.7}$$

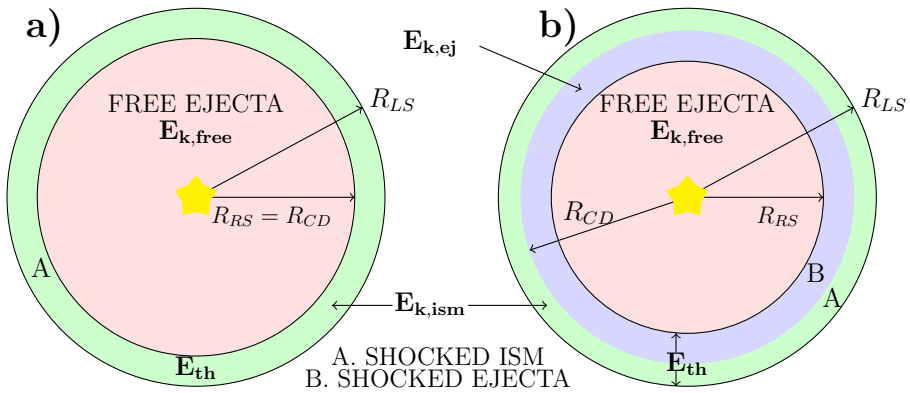

Figure 3.1: Sketch of the proposed model for the ED-phase. **a)** The initial condition at $t = t_0$ for a remnant in the ED-phase. **b)** The SNR structure for any $t > t_0$. See the text for a discussion on the labels of this scheme.

The independent parameters are $\{E_0, M_{ej}\}$. The explosion releases a total energy E_0, which is assumed to be all as kinetic energy of the ejected gas. Therefore the free-expansion velocity v_{ej} depends on the value of these input parameters through the equation:

$$E_0 = \frac{1}{2} M_{ej} v_{ej}^2 \int_0^1 4\pi w^4 f(w)\, dw. \tag{3.2.8}$$

Ejecta energies

To apply the Thin-Shell approximation (TSA) to the early evolution of SNRs, it is necessary to calculate the thermal pressure behind the leading shock at R_{LS}. The main assumptions to extend the TSA to the ED-Phase are: the reverse shock is spherical with radius R_{RS} and velocity V_{RS} in the rest frame. Second, following Silich & Tenorio-Tagle (2018), the thermal pressure is assumed to be uniform in the region between the two shocks, with a small fall (to be discussed in section 3.5) just behind the reverse shock. Finally, the shocked ambient gas and the shocked ejecta move with the same velocity.

In order to determine the reverse shock dynamics, one has to consider additional energy terms in the energy conservation equation. At early times, most of the total

energy E_0 is in the form of kinetic energy of the ejecta $E_{k,free}$:

$$E_{k,free} = \frac{1}{2} M_{ej} v_{ej}^2 \left(\frac{3-n}{5-n}\right) \left(\frac{R_{RS}}{t v_{ej}}\right)^{5-n}. \tag{3.3.1}$$

As the leading shock expands into the ambient gas, the kinetic energy of the free ejecta starts to decrease while being converted into kinetic energy of the shocked ejecta $E_{k,ej}$, kinetic energy of the ambient swept-up gas $E_{k,ism}$ and thermal energy E_{th} of all the gas located between the two shock surfaces.

The shocked ejecta is separated from the shocked ambient gas by a contact discontinuity R_{CD}. Fig 3.1b shows a sketch of the SNR structure at this stage. Under the assumptions adopted for this model, the kinetic energy of the shocked ejecta is:

$$E_{k,ej} = \frac{1}{2} M_{th} U^2. \tag{3.3.2}$$

In this expression M_{th} is the mass of the thermalized ejecta:

$$M_{th} = M_{ej} \left[1 - \left(\frac{R_{RS}}{v_{ej} t}\right)^{3-n}\right], \tag{3.3.3}$$

and U is the gas velocity behind the leading shock. $E_{k,ism}$ is calculated as in the previous chapter:

$$E_{k,ism} = \frac{1}{2} \int \int \mu U^2 d\lambda_1 d\lambda_2. \tag{3.3.4}$$

If radiative losses are negligible, the energy conservation equation yields:

$$E_0 = E_{k,free} + E_{k,ej} + E_{th} + E_{k,ism}. \tag{3.3.5}$$

From this equation it is possible to calculate E_{th} at every instant of time if R_{RS} and V_{RS} are known. The thermal pressure between the two shocks is:

$$P = (\gamma - 1) \frac{E_{th}}{\Omega_{LS} - \Omega_{RS}}, \tag{3.3.6}$$

where Ω_{LS} and Ω_{RS} are the volumes enclosed by the leading and the reverse shocks,

respectively. Equations 3.3.6 assumes that the thermal pressure is uniform between the leading and the reverse shock, which is a good approximation as P falls only in a narrow region behind the reverse shock.

Setting the Initial Conditions

At the initial time t_0, the values of E_0, M_{ej} and n must be selected. With these values the free-expansion velocity v_{ej} is obtained from equation 3.2.8.

At t_0 it is assumed that a small fraction β (usually $\beta < 5\%$) of the energy E_0 has been already transformed into $E_{k,ism}$, E_{th} and $E_{k,ej}$. In order to determine the maximum velocity of the ejecta at the initial position of the reverse shock V_{max}, one has to note that (see equation 3.3.1):

$$E_{k,free} = \frac{1}{2} M_{ej} v_{ej}^2 \left(\frac{3-n}{5-n}\right) \left(\frac{v}{v_{ej}}\right)^{5-n}. \tag{3.4.1}$$

Therefore, at the initial time:

$$(1-\beta)\, E_0 = \frac{1}{2} M_{ej} v_{ej}^2 \left(\frac{3-n}{5-n}\right) \left(\frac{V_{max}}{v_{ej}}\right)^{5-n}. \tag{3.4.2}$$

Taking into account that:

$$E_0 = \frac{1}{2} M_{ej} v_{ej}^2 \left(\frac{3-n}{5-n}\right), \tag{3.4.3}$$

one can obtain:

$$V_{max} = v_{ej} \left(1-\beta\right)^{1/(5-n)}. \tag{3.4.4}$$

Following Truelove & McKee (1999), Chevalier (1982a), Hamilton & Sarazin (1984), or Hwang & Laming 2012, let us define the leading factor:

$$l\,(t) = \frac{R_{LS}}{R_{RS}}, \tag{3.4.5}$$

and the value of the leading factor at the initial time t_0 as:

$$l_{ED} = l\left(t_0\right), \tag{3.4.6}$$

then:

$$R_{LS}\left(t_0\right) = l_{ED} R_{RS}\left(t_0\right). \tag{3.4.7}$$

It is assumed that at the initial time t_0, the position of the reverse shock coincides with the contact discontinuity (TM99) (see Fig. 3.1a):

$$R_{LS}\left(t_0\right) = l_{ED} R_{CD}\left(t_0\right). \tag{3.4.8}$$

Then:

$$V_{LS}\left(t_0\right) = l_{ED} v_{max}, \tag{3.4.9}$$

where $V_{LS}\left(t_0\right)$ is the velocity of the leading shock at t_0. The value of l_{ED} is calculated from equation 3.4.8 and mass conservation. Indeed, assuming that at $t = t_0$ the post-shock density is uniform and 4 times larger than the density of the unshocked ambient gas, mass conservation yields:

$$\left(R_{LS}^3\left(t_0\right) - R_{CD}^3\left(t_0\right)\right) 4\rho_0 = R_{CD}^3\left(t_0\right)\rho_0, \tag{3.4.10}$$

this implies $l_{ED} = 1.1$. The initial velocity of the shocked ISM then is:

$$U_{ini} = \frac{2}{\gamma + 1} l_{ED} V_{max}. \tag{3.4.11}$$

Finally, the shock positions are determined from equation 3.4.7 and the energy conservation equation. As β is the fraction of the ejecta kinetic energy converted into other energies, the energy conservation equation reads:

$$\beta E_0 = E_{k,ism}^0 + E_{th}^0 + E_{k,ej}^0, \tag{3.4.12}$$

where the terms on the right-hand side of this expression are the thermal and kinetic energies of the shocked ejecta and the shocked ISM at time t_0:

$$E^0_{k,ism} = \frac{1}{2}\rho_0 \frac{4\pi}{3} R^3_{LS}\left(t_0\right)\left(\frac{2}{\gamma+1} l_{ED} V_{max}\right)^2, \tag{3.4.13}$$

$$E^0_{k,ej} = \frac{1}{2} M_{ej}\left[1-\left(\frac{V_{max}}{v_{ej}}\right)^{3-n}\right]\left(\frac{2}{\gamma+1} l_{ED} V_{max}\right)^2, \tag{3.4.14}$$

$$E^0_{th} = \frac{4}{\gamma-1}\frac{k\rho_0}{\mu} T_{shock}\frac{4\pi}{3}\left(1-\frac{1}{l^3_{ED}}\right) R^3_{LS}\left(t_0\right). \tag{3.4.15}$$

Here , T_{shock} is the post-shock temperature behind the leading shock, assuming that the post-shock density is $4n_0$. Note that in equations (3.4.13-3.4.15) the only unknown parameter is R_{LS}. The initial position for the leading shock radius $R_{LS}\left(t_0\right)$ is calculated by making use of equation 3.4.12 together with equations (3.4.13-3.4.15). Finally, $R_{RS}\left(t_0\right)$ is obtained from equation 3.4.7.

The Reverse Shock Position

The position and velocity of the reverse shock are determined by making use of the Rankine-Hugoniot relations. In the frame of the unschocked ejecta, the shock velocity is (Zel'dovich & Raizer, 2012):

$$\tilde{V}^2_{RS} = \frac{\gamma+1}{2}\frac{P_{RS}}{\rho_{ej}}, \tag{3.5.1}$$

where P_{RS} is the pressure behind the reverse shock and ρ_{ej} is the density of the freely expanding ejecta. In the rest frame the shock velocity is given by:

$$V_{RS} = \frac{R_{RS}}{t} - \tilde{V}_{RS}. \tag{3.5.2}$$

As stated in section 3.3, the thermal pressure falls behind the reverse shock (Silich & Tenorio-Tagle, 2018). Therefore, it is expected that $P_{RS} < P$. To understand the relation between P_{RS} and the remnant pressure P (calculated in equation 3.3.6), let

us define the pressure ratio ϕ between the leading and the reverse shock as (TM99):

$$\phi = \frac{P_{RS}}{P} = \frac{\rho_{ej}\left(R_{RS}/t, t\right)\tilde{V}_{RS}^2}{\rho_0 V_{LS}^2}. \tag{3.5.3}$$

A uniform pressure between the two shocks would imply $\phi = 1$, but several calculations (e.g. Gull 1973, Gull 1975, Chevalier 1982b, McKee & Truelove 1995, Hamilton & Sarazin 1984, Silich & Tenorio-Tagle 2018) show that $\phi < 1$. For example, both for steep power-law ejecta (Chevalier, 1982a) and uniform ejecta (Hamilton & Sarazin, 1984): $\phi = 0.3$. In fact, as it is shown in Appendix A, the adopted initial conditions for this work (see subsection 3.4) require the pressure ratio to be $\phi \approx 0.3$ at the initial time t_0. Moreover, in this appendix is also shown that when the reverse shock reaches the center of the explosion, i.e., when the remnant enters the Sedov-Taylor phase: ϕ is also equal to 0.3 (Gaffet, 1978).

A precise knowledge of ϕ is complex and it is beyond the scope of our approximation. But, given the fact that at early and late times ϕ is approximately 0.3 and taking into account that numerical simulations have shown that ϕ is a slowly varying function of time (e.g. McKee & Truelove 1995, Fabian et al. 1983), hereafter it is assumed that $\phi = 0.3$.

Discussion

Density and Temperature profiles for a SNR produced by a uniform density ejecta

To test the method discussed above, let us consider a SN explosion with $E = 10^{51}$ erg and $M_{ej} = 3$ M$_\odot$ that occurs in an ISM with $n_0 = 1$ cm^{-3}. First, lets considered the case of an ejecta with a uniform density (i.e., index $n = 0$).

The method proposed in this work allows to determine the position of the leading R_{LS} and reverse R_{RS} shocks for the entire evolution. Under certain assumptions, it is also possible to estimate the position of the contact discontinuity R_{CD} and the densities and temperatures of the region between the two shocks.

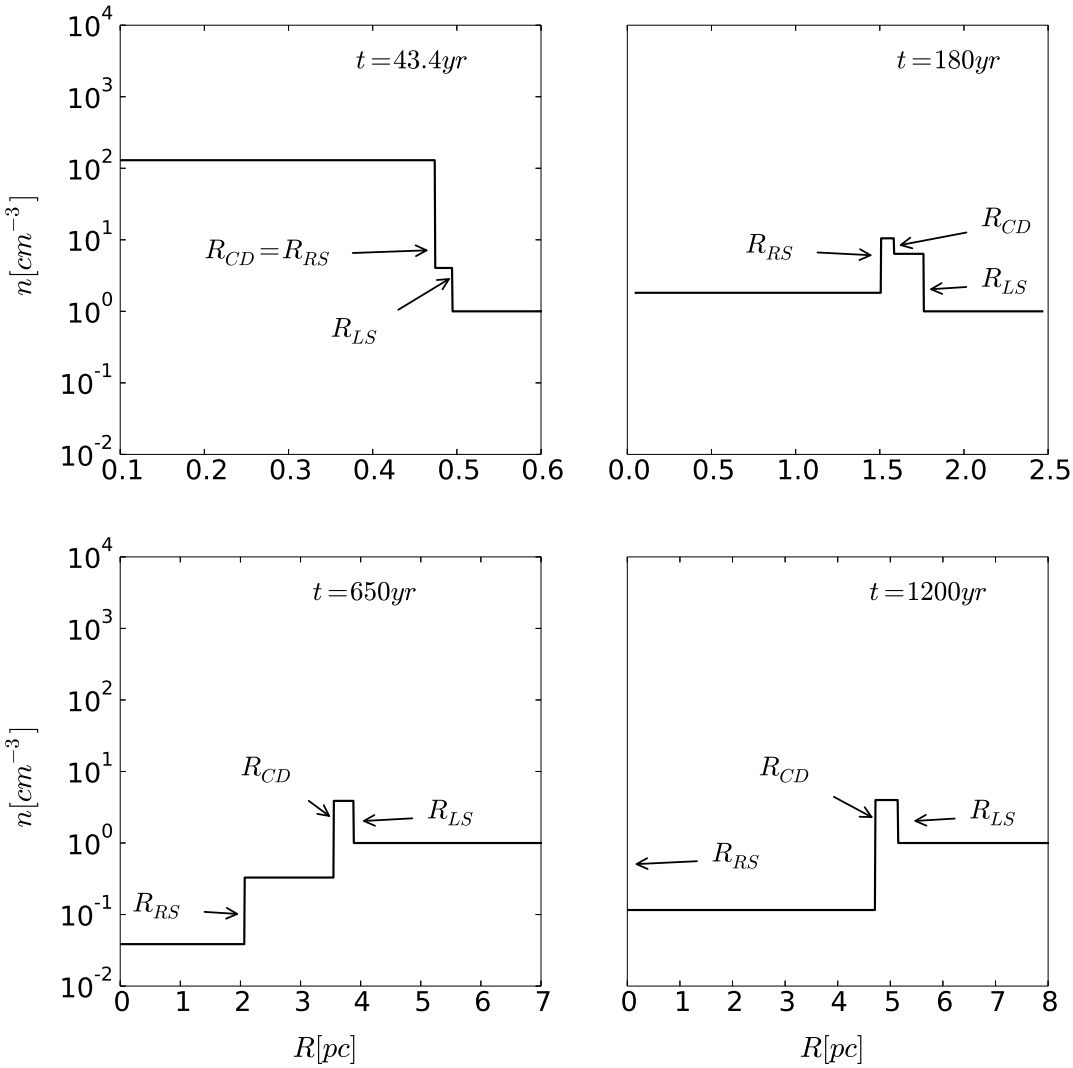

Figure 3.2: *The SNR density structure for a uniform density ejecta. The x-axis is normalized with the value of R_{LS} at the time of the snapshot. The top left panel shows the initial condition. The existence of shocks is revealed by the density jumps. As time advances, the reverse shock rapidly converges towards the center of the explosion.*

Let us assume that the mass M overtaken by R_{LS} is concentrated in a shell of uniform

temperature equal to the post-shock temperature and a uniform pressure P. The width ΔR of this shell and therefore the position of R_{CD} can be calculated as:

$$\Delta R = \frac{M}{d\Sigma \rho_{shell}}, \tag{3.6.1}$$

where:

$$\rho_{shell} = \frac{\mu P}{k T_{shock}}. \tag{3.6.2}$$

In these equations, k is the Boltzmann constant, P the remnant Pressure, and $d\Sigma$, T_{shock}, M are the surface area, post-shock temperature and mass of the shell, respectively. These variables are known at every time step. ΔR is obtained from equation 3.6.1 and hence the value of R_{CD}.

The density of the shocked ejecta is estimated as a mean density:

$$\rho_{s,ej} \approx \frac{3 M_{th}\left(R_{RS}, t\right)}{4\pi\left(R_{CD}^3 - R_{RS}^3\right)}, \tag{3.6.3}$$

where M_{th} is the thermalized mass (calculated using equation 3.3.3). The temperature of the shocked ejecta is calculated from equation 3.6.3 and the equation of state such that the pressure of this region is equal to the remnant pressure P.

Under these assumptions, Fig. 3.2 and 3.3 show the density and temperature evolution during the ED-phase calculated with the initial conditions fixed for this test. The top left panel of both figures correspond to the initial condition, where the reverse shock coincides with the contact discontinuity (see Fig. 3.1).

Note that this figure makes clear that during the early evolution, the ejecta mass dominates over the swept-up mass. As time advances, the reverse shock (located at the density jump) starts to accelerate inwards and at $t \approx 1000$ yr reaches the center of the explosion. Fig 3.3 shows the temperature structure. After the reverse shock has reached the center, the remnant interior is diffuse and hot (see right bottom panels of Figs. 3.2 and 3.3), as stressed in previous works (e.g., LeVeque et al. 2006, Cioffi et al. 1988b).

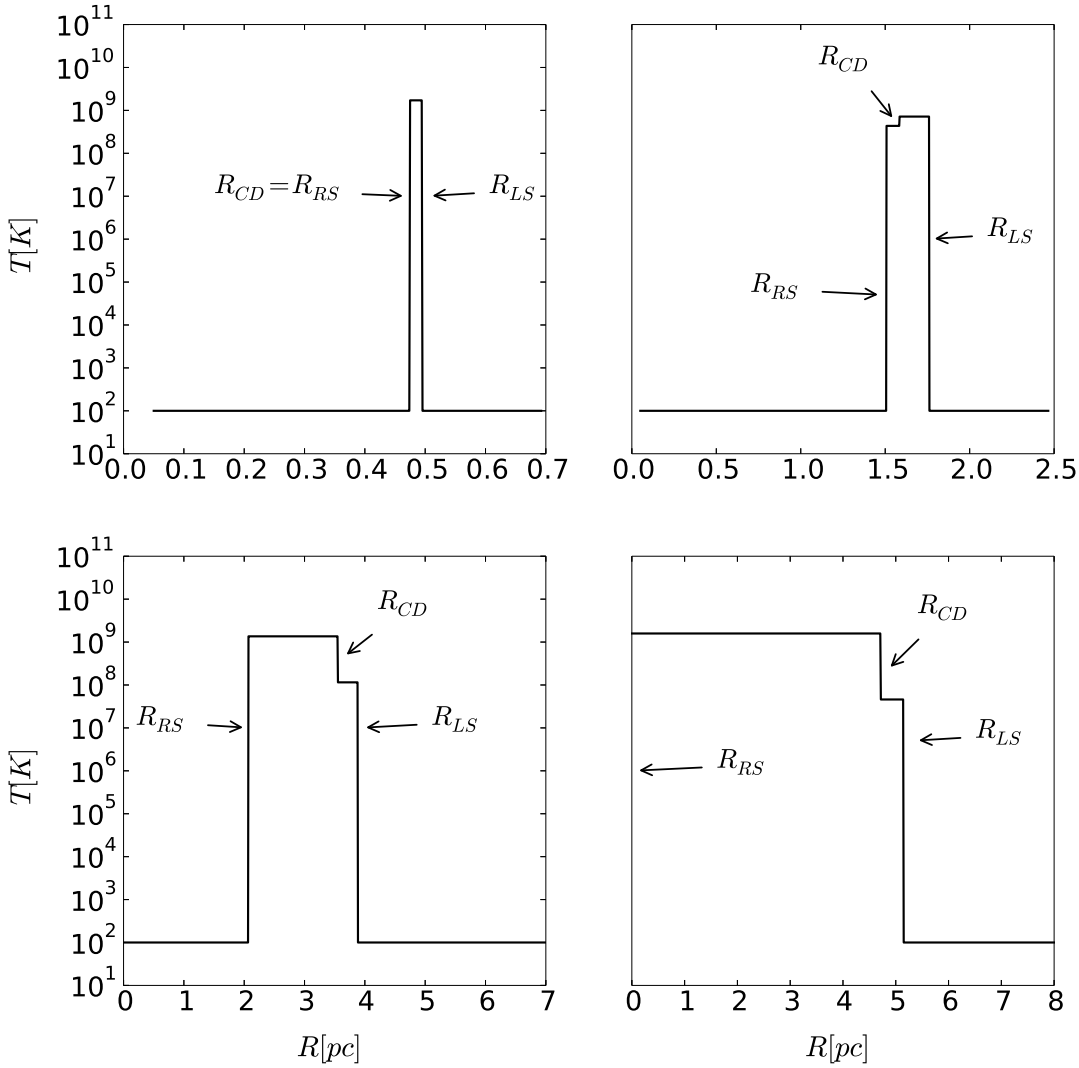

Figure 3.3: *Same as Fig. 3.2 but for the gas temperature.*

Impact of the ejecta density distribution on the evolution of SNRs

Fig.3.4 compares the reverse and leading shocks positions for ejecta with different density distributions ($n = 0$ and $n = 2$). The reverse shock moves outwards until

both the thermal and ram pressures of the free ejecta become small enough, to drive the shock back towards the origin of the explosion. Note that it takes a longer time for the reverse shock to reach the center of the explosion for the case $n = 2$. This is because in this case more of the ejecta mass is located in the central zone and the density ahead of the reverse shock increases at smaller radii as $\rho \propto r^{-2}$. Therefore in the case when $n = 2$, the reverse shock velocity is smaller than in the case when $n = 0$.

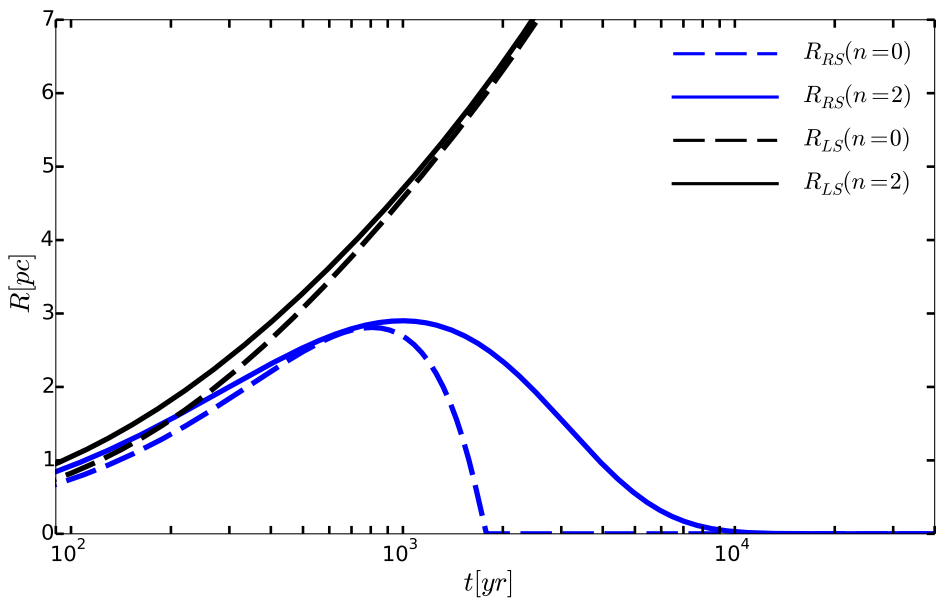

Figure 3.4: *Leading and reverse shocks for $n = 0$ (dashed lines) and a power-law $n = 2$ (solid lines) density distributions.*

The evolution of the energies is shown in Fig. 3.5. As mentioned before, initially most of the explosion energy is concentrated in the kinetic energy of the cold ejecta. At late times all of it has been transformed into the thermal and kinetic energy of the shocked ISM and shocked ejecta. For the uniform density ejecta ($n = 0$), there is more mass in the outer part of the remnant and therefore $E_{k,ej}$ is bigger in this case than in the power-law density case (bottom left panel on Fig. 3.5). Note that at $t \approx 2 \times 10^3$ yr, the energies calculated for $n = 0$ and $n = 2$ begin to converge. The convergence is also

noticeable in Fig. 3.4, for the leading shocks. This implies that the long term SNRs dynamical evolution is insensitive to the initial structure of the SN ejecta. Fig. 3.6 shows the global kinetic and thermal energies of the remnant. Here the kinetic energy has been defined as the sum of $E_{k,ej}$, $E_{k,ism}$ and $E_{k,free}$. This figure explains why some authors name the ED-phase as the *thermalization epoch*. The original kinetic energy of cold ejecta is transformed into thermal and kinetic energy of the hot gas.

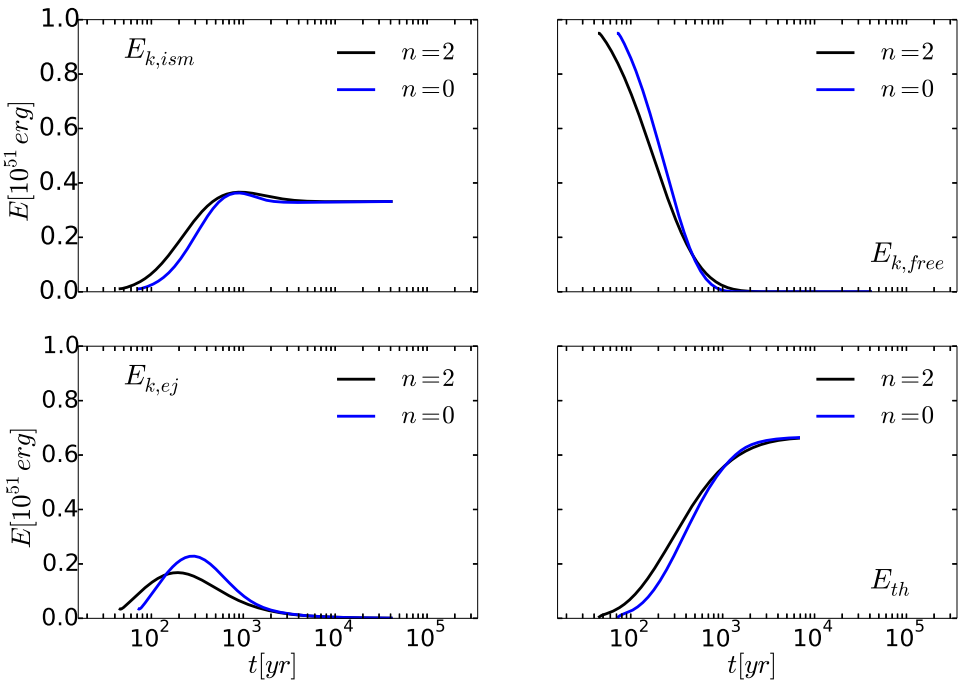

Figure 3.5: *Evolution of energies at early SNR evolution. The black lines correspond to the case $n = 2$ and the blue lines to the case $n = 0$.*

Comparison with analytical results

This section compares the outcome of the thin-shell code with the results of TM99, who obtained expressions for the position and velocity of both the reverse and leading shocks, from the early ejecta-dominated stage to the Sedov-Taylor phase[1]. Our results for the leading shock R_{LS} is compared with those obtained by TM99 in Fig. 3.7. As

[1]see appendix B for a review.

one can see, our result is in excellent agreement with the analytic prediction[2] (errors $\leq 5\%$). The reverse shock position coincides with the numerical result of TM99 even better than their analytic formula, as can be seen in Fig. 3.8.

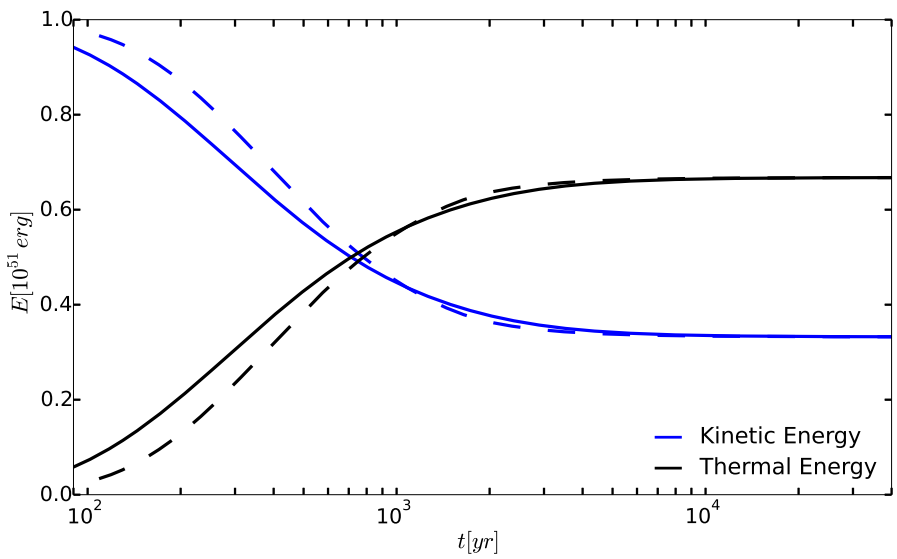

Figure 3.6: *Total kinetic and thermal energies of a SNR during the ED-phase for a uniform density ejecta (dashed lines) and a power-law ejecta $n = 2$ (solid lines).*

Summary

A method based on the energy conservation equation has been developed. This method allows one to study the dynamics and evolution of supernova remnants from the ejecta-dominated stage to the Sedov-Taylor stage. It was shown that the long term evolution of SNRs does not depend on the specific conditions of the ejected material. The result of calculations were compared with previous analytic and numerical results and it was found a good agreement for the dynamics of both shocks.

[2]And therefore, also in excellent agreement with the numerical result, as the formula obtained by TM99 for R_{LS} follows closely the results of their numerical calculation.

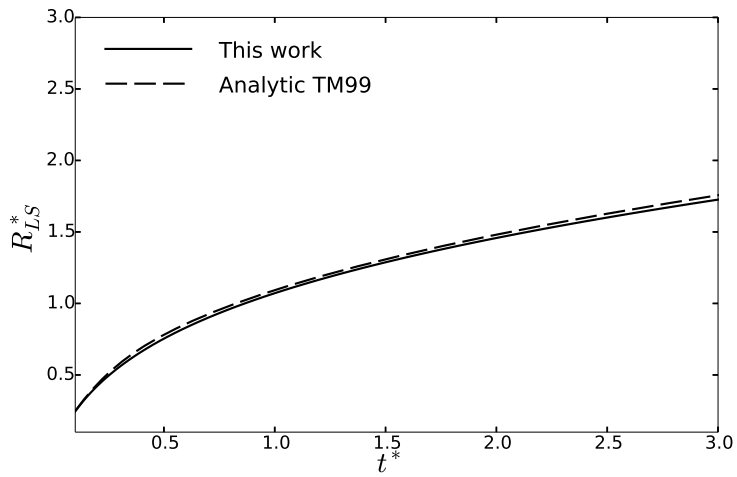

Figure 3.7: *Comparison of the leading shock radius. The solid line is the value calculated in this work and the dashed line is the result of TM99. The starred variables at the axis are dimensionless variables as defined in TM99 (see Appendix B).*

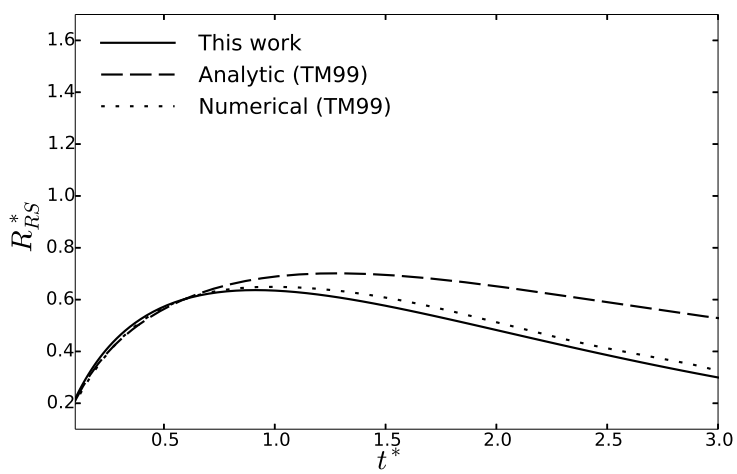

Figure 3.8: *Comparison of the reverse shock radius. The solid line is the value calculated in this work, the dashed and dotted lines are the analytic and numerical results of TM99, respectively. The starred variables at the axis are dimensionless variables as defined in TM99 (see Appendix B).*

Chapter 4

Effects of radiative cooling on the evolution of SNRs

Introduction

During the Sedov-Taylor stage (ST), the shocked gas is heated to high temperatures as the shock velocity is large ($T \propto V^2$) and radiative losses of energy behind the leading shock are thus negligible. However, the shock velocity and the shocked gas temperature become smaller with time. This leads to enhanced radiative cooling. After the end of the ST stage, the remnant further evolves in the Snowplough regime (e.g., Terlevich et al. 1992, Cioffi et al. 1988b, Petruk 2006, Blondin et al. 1998).

The dynamical evolution of a SNR at the snowplough phase is dominated by the radiative losses of energy. During this phase, all the swept-up gas collapses into a cold shell. The purpose of this chapter is to include the effects of radiative cooling into the Thin-Shell code.

The cooling Function

The rate of radiative cooling is determined by the gas density, temperature and the chemical composition (e.g., Raymond et al. 1976, Wiersma et al. 2009, Schure et al. 2009). In the case of collisional ionization equilibrium (CIE), the cooling rate L_R is

determined by a cooling-function $\Lambda(T, Z)$ (where Z is the gas metallicity):

$$L_R = \int n_i n_e \Lambda(T, Z)\, d\Omega. \tag{4.2.1}$$

In equation 4.2.1, n_i and n_e are the gas ion and electron number densities, respectively. In the case of a completely ionized plasma, $n_i = n_e = n$ and the cooling rate is:

$$L_R = \int n^2 \Lambda(T, Z)\, d\Omega, \tag{4.2.2}$$

The cooling function is the result of several radiative processes: recombination, collisional excitation and free-free emission. Fig. 4.1 shows the cooling function calculated for a gas in Collisional Ionization Equilibrium (CIE) and a solar metallicity. The solid and dotted black lines are the results of Raymond et al. (1976) and Wiersma et al. (2009), respectively. The contribution of individual chemical elements to the cooling function is shown in color lines.

At low temperatures $T < 10^4$ K, the radiative cooling is inefficient and depends on the degree of ionization. In the temperature range 10^4 K$< T < 10^{6.5}$ K, cooling is strong due to line emission from elements as H, He, C, O, Si and Fe. At $T \approx 3 \times 10^7$ K, all the atoms become fully ionized and the cooling function drops to a local minimum value. At higher temperatures, the cooling is produced mainly by free-free radiation. Hereafter, the CIE cooling function from Raymond et al. (1976) is used for our calculations and it is assumed that $n_i = n_e$.

Model equations

The thin shell-formation time

Let us define the *thin shell-formation time* t_{sf} as the time when a cold, dense shell is formed and the SNR enters the snowplough stage. The shocked gas cools and in order to compensate for the lost of temperature and to keep a similar pressure to that of the shocked ejecta, it collapses into a thin dense shell. If an element of the gas is

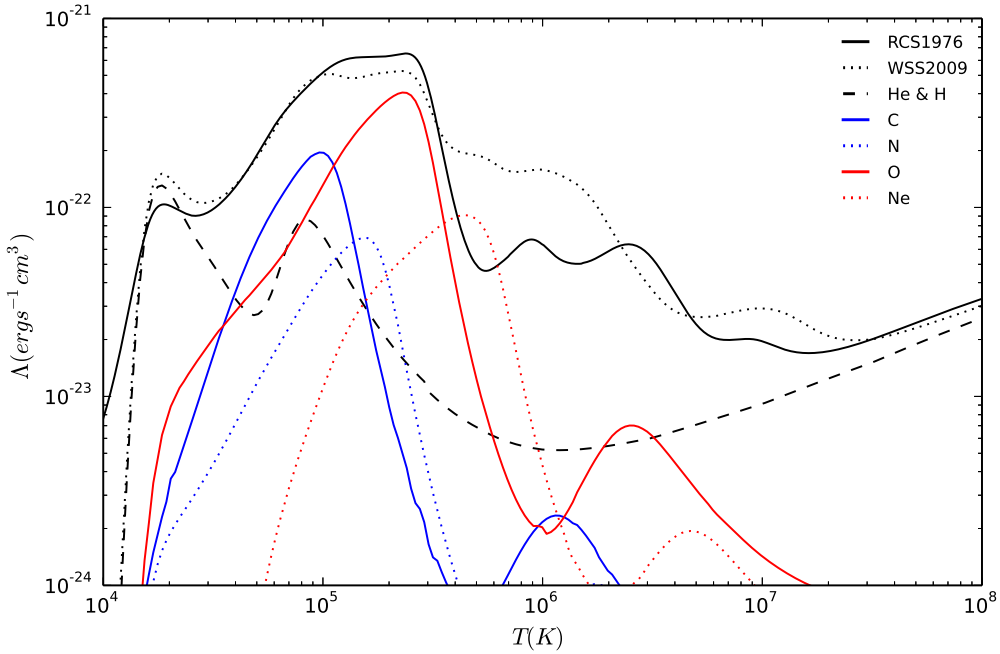

Figure 4.1: *Collisional Ionization Equilibrium (CIE) cooling function. The black dotted line is the result of Wiersma et al. (2009) and the solid black line is taken from Raymond et al. (1976). The contribution to the cooling function due to several chemical elements is also shown.*

shocked at time t, it cools at:

$$t_c = t + \Delta t_{cool}\left(t\right), \tag{4.3.1}$$

where $\Delta t_{cool}\left(t\right)$ is the gas cooling time (e.g. (Kim & Ostriker, 2015, hereafter KO15):

$$\Delta t_{cool}\left(t\right) = \frac{1}{\gamma+1}\frac{k_B T_{shock}}{n_0 \Lambda\left(T_{shock}\right)}. \tag{4.3.2}$$

In this expression, k_B is the Boltzmann constant, T_{shock} is the post-shock temperature, n_0 is the density of the unshocked medium and γ is the ratio of specific heats. In our simulations t_c is calculated at each time-step and the minimum t_{min} is determined:

$$t_{min} = min\left(t_c\left(t\right), t_c\left(t+\Delta t\right), \ldots\right). \tag{4.3.3}$$

The transition time t_{sf} to the Snowplough regime occurs when the time t is larger than t_{min}. Fig. 4.2 shows the shell formation time calculated with the Thin-Shell code for SNRs evolving into an ambient medium with different densities. This figure presents also a comparison with previous results.

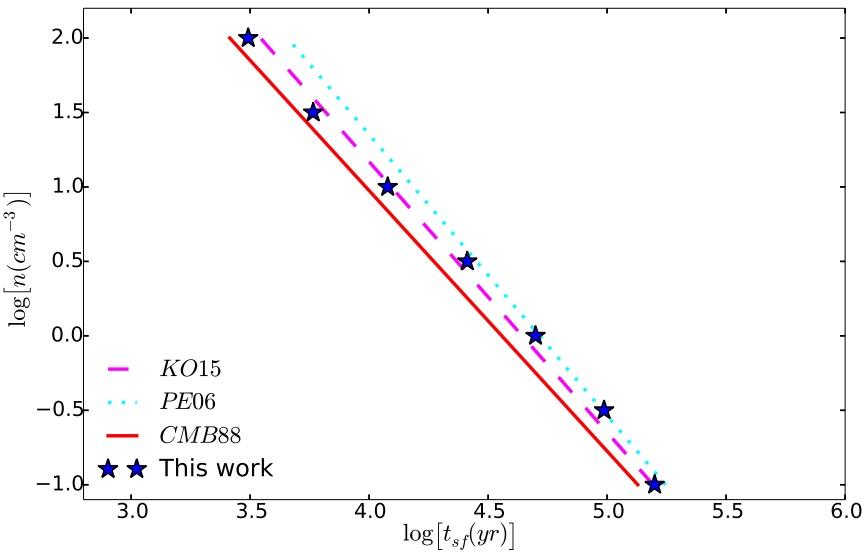

Figure 4.2: *The shell formation time t_{sf} as a function of the ambient gas density. The star symbols presents values calculated with the Thin-shell Code. The red solid curve, the magenta dashed and the cyan dotted curves show characteristic cooling times calculated by (Cioffi et al., 1988a, hereafter CMB88), KO15 and (Petruk, 2006, hereafter PE06), respectively.*

The energy equation

The SNR dynamics are determined by the set of equations presented in chapter 2. However, radiative cooling changes the equation of energy. During the Sedov-Taylor stage, radiative losses of energy are negligible. Here, however, radiative cooling is introduced into the energy conservation equation to study the transition from the ST to the Snowplough stage.

The swept-up mass is assumed to be contained in a shell with uniform temperature (equal to the post-shock temperature, i.e., $T_{shell} = T_{shock}$) and uniform pressure (equal to the uniform remnant pressure $P_{shell} = P$). T_{shock} is calculated from the adiabatic Rankine-Hugoniot relations.

The remnant consist of a hot central bubble surrounded by the shell of swept up matter. In the Thin-shell approximation, the mass and therefore the kinetic energy are concentrated in the shell $E_{k,shell}$. The total thermal energy E_{th} includes the thermal energy of the central bubble $E_{th,b}$ and the thermal energy of the shell $E_{th,shell}$:

$$E_{th} = E_{th,shell} + E_{th,b}. \tag{4.4.1}$$

$E_{th,b}$ changes due to the expansion of the hot gas located inside a volume encompassed by the contact discontinuity:

$$\frac{dE_{th,b}}{dt} = -Pd\Omega. \tag{4.4.2}$$

The energy lost by the bubble is transferred to the shell, which also losses energy by radiation. Therefore, the total energy of the shell $E_{tot,shell}$ changes as:

$$\frac{dE_{tot,shell}}{dt} = \frac{dE_{th,shell}}{dt} + \frac{dE_{k,shell}}{dt} = Pd\Omega - \sum_{i,j} n^2_{shell,i,j}\Lambda\left(T_{shock}\right)\Omega_{i,j}. \tag{4.4.3}$$

In equation 4.4.3, the shell number density and volume are given by:

$$n_{shell,i,j} = \frac{\rho_{shell,i,j}}{\mu m_H} = \frac{P}{k_B T_{shock} m_H}, \tag{4.4.4}$$

$$\Omega_{i,j} = \frac{M_{i,j}}{\rho_{shell,i,j}}. \tag{4.4.5}$$

In these equations, m_H is the proton mass and $M_{i,j}$ is the mass of the Lagrangian element (i, j). Combining equations 4.4.2 and 4.4.3 and taking into account equation 4.4.1, one can obtain:

$$\frac{dE_{th}}{dt} = -\sum_{i,j} n^2_{shell,i,j}\Lambda\left(T_{shock}\right)\Omega_{i,j} - \frac{dE_{k,shell}}{dt}. \tag{4.4.6}$$

The total remnant energy E_{total} is:

$$E_{total} = E_k + E_{th}. \tag{4.4.7}$$

At the initial time t_0, E_{total} is equal to the explosion energy:

$$E_{total}\left(t_0\right) = E_0. \tag{4.4.8}$$

Table 4.1: SNR parameters measured at the shell formation time t_{sf}. Column 1 is the fixed number density of the ambient gas. Second column: t_{sf} calculated with the thin-shell code compared with the result from KO15 in parenthesis. Columns 3 to 6: shock radius, post-shock temperature, swept-up mass and remnant momentum calculated in this work compared with the respective results from KO15 shown in parenthesis.

n cm^{-3}	t_{sf} 10^3 yr	R_{sf} pc	T_{sf} 10^6 K	M_{sf} 10^3 M$_\odot$	$\vec{p}_{sf}$ 10^5 M$_\odot$ km s^{-1}
0.1	158(150)	58.4(58.5)	0.26(0.31)	2.60(2.96)	2.69(2.78)
1.0	50(41.9)	23.2(22.5)	0.41(0.57)	1.64(1.68)	2.10(2.05)
10.0	11.8(10.6)	8.25(8.34)	0.91(1.04)	0.74(0.85)	1.42(1.43)
100.0	3.10(2.63)	3.04(3.03)	1.82(1.90)	0.37(0.41)	1.0(0.97)

Results

To verify the method discussed in the previous subsections, 4 cases for the density of the ambient medium: $n_0[\mathrm{cm}^{-3}] = 0.1, 1, 10, 100$ have been considered. This permits us to compare our results with the ones obtained in recent high resolution hydrodynamic simulations carried out by Kim & Ostriker (2015) and Li et al. (2015).

Table 4.1 shows the values of different physical quantities of the remnant calculated at t_{sf}. These results are compared (in parenthesis) with the numerical values obtained from KO15. From this table one can see that our results are in reasonable agreement with the results of numerical calculations.

Fig. 4.3 shows the evolution of kinetic, thermal and total energies during the transition from the Sedov-Taylor to the snowplough stage. One can note that at this stage the thermal energy of the remnant changes more rapidly than the kinetic one, as already has been mentioned in previous calculations (e.g. Thornton et al. 1998, Kim & Ostriker 2015, Haid et al. 2016, Li et al. 2015).

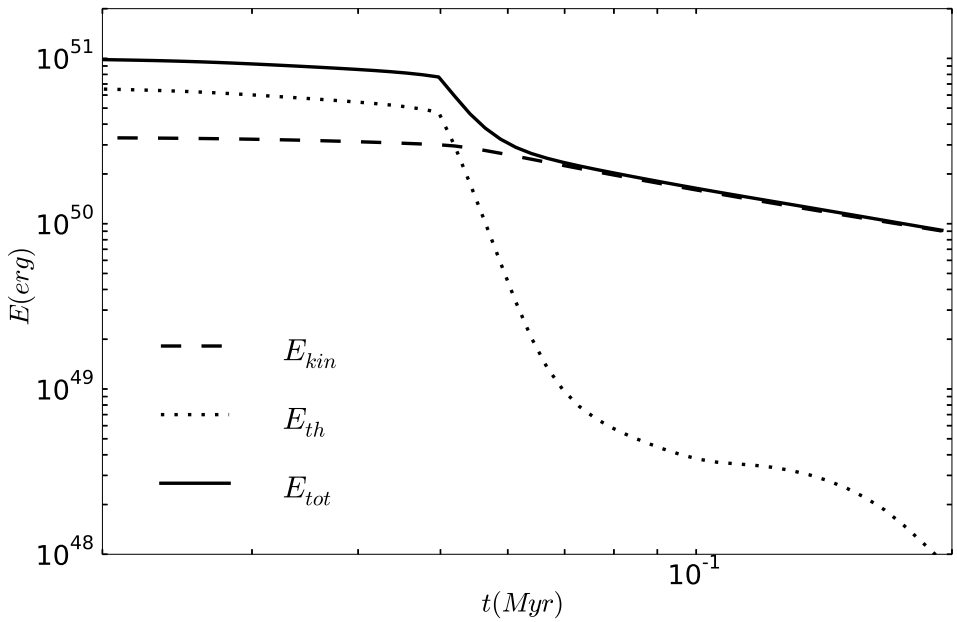

Figure 4.3: *Evolution of thermal, kinetic and total energies for a SNR that evolves into an ISM with density $n = 1\ cm^{-3}$ and undergoes the transition from ST to the Snowplough stage.*

Finally, as has long been known, the shock radius is well described by power-laws $R \propto t^{\beta}$ both during the Sedov-Taylor and the Snowplough stages. During the ST, the analytic solution yields $\beta_{ST} = 0.4$, whereas at the Snowplough stage, $\beta_{SP} \approx 0.3$ (see Draine & McKee 1993, Kim & Ostriker 2015, Li et al. 2015).

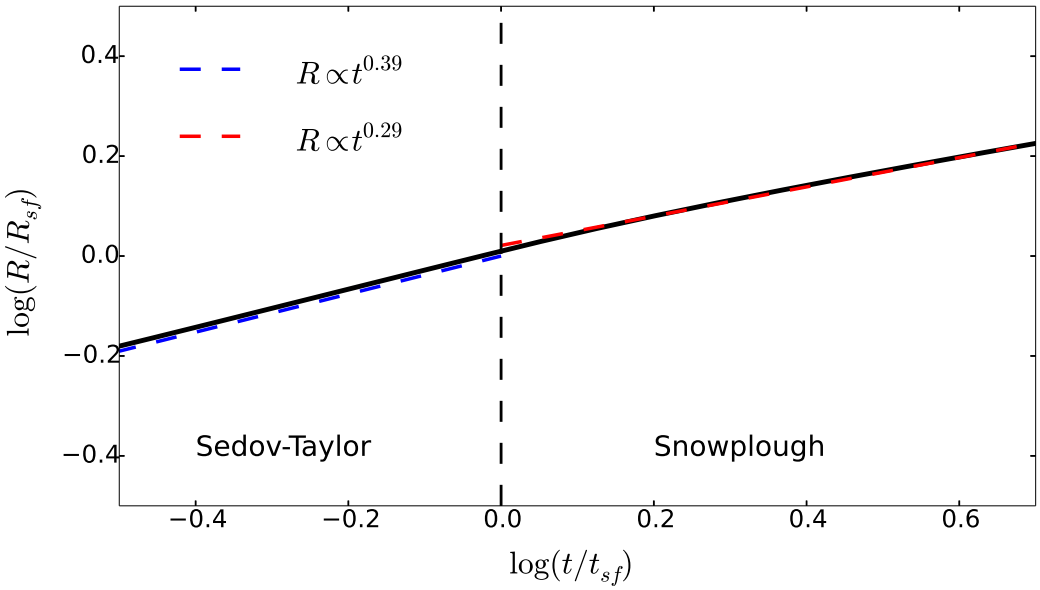

Figure 4.4: *Power-law fitting to the shock radius both during the ST stage (blue dashed line) as during the Snowplough stage (red dashed line). Our results are in excellent agreement with those in the literature.*

The shock radius obtained with the Thin-Shell code is shown in Fig. 4.4. The color dashed lines shows the power-law fitting to the radius for both stages. Our results are $\beta_{ST} = 0.39$ and $\beta_{SP} = 0.29$, which are in excellent agreement with the results of Kim & Ostriker (2015) and Li et al. (2015).

Summary

In this chapter, the Thin-Shell method described in previous chapters was modified in order to take into account strong radiative cooling that occurs at late stages of the SNRs evolution. The numerical method was compared with recent numerical results and a good agreement was found.

Chapter 5

Evolution of SNRs in different ambient densities

Introduction

The previous chapters have addressed different stages of the SNR evolution and how to implement and accurately calculate them by means of the Thin-Shell approximation. The aim of this chapter is to merge these results to construct a complete picture of the SNR evolution including also different environments.

The energy conservation equation

If radiative losses of energy are negligible, the equation of energy conservation during the ejecta-dominated (ED) stage is (see chapter 3):

$$E_0 = E_{k,free} + E_{k,ej} + E_{th} + E_{k,ism}, \tag{5.2.1}$$

where E_0 is the explosion energy, E_{th} is the total thermal energy and $E_{k,free}$, $E_{k,ej}$, $E_{k,ism}$, are the kinetic energies of the free ejecta, the shocked ejecta and the shocked ambient gas, respectively. Equation 5.2.1 was used in chapter 3 to calculate the thermal pressure $P(t)$ between the leading and the reverse shocks. This, in turn, allowed us to follow the dynamical evolution of the leading and the reverse shocks.

After full thermalization of the SN ejecta, this equation reduces to (see chapter 4):

$$E_0 = E_{th} + E_{k,ism} + E_{rad}. \tag{5.2.2}$$

In equation 5.2.2, E_{rad} is the energy lost by radiation due to cooling of the shocked ambient gas.

In order to follow the complete evolution of SNRs taking into account all possibilities of gas cooling, an additional radiation term for the shocked ejecta must be included into the energy conservation equation. Therefore, equation 5.2.1 is generalized as:

$$E_0 = E_{k,free} + E_{k,ej} + E_{th} + E_{k,ism} + E_{rad1} + E_{rad2}, \tag{5.2.3}$$

where E_{rad1} and E_{rad2} are the amounts of energy lost by radiation at the outer and inner shells, respectively. Equation 5.2.3 can be written in a differential form:

$$\frac{dE_{th}}{dt} = -\frac{dE_{k,free}}{dt} - \frac{dE_{k,ej}}{dt} - \frac{dE_{k,ism}}{dt} - Q_1 - Q_2, \tag{5.2.4}$$

where:

$$Q_1 = \frac{dE_{rad1}}{dt}, \quad Q_2 = \frac{dE_{rad2}}{dt}, \tag{5.2.5}$$

are the rates of energy radiated by the shocked ambient gas and the shocked ejecta, respectively.

The time derivatives of the kinetic energies $E_{k,free}$, $E_{k,ej}$ and $E_{k,ism}$ can be calculated by means of equations 3.3.4, 3.3.1 and 3.3.2. The cooling rates Q_1 and Q_2 could be calculated as proposed in chapter 4. The cooling time $\Delta t_{cool,1}$ and $\Delta t_{cool,2}$ for the outer and inner shells are:

$$\Delta t_{cool,1}(t) = \frac{\mu}{\gamma+1}\frac{k_B T_{LS}}{\rho_0 \Lambda(T_{LS})}, \tag{5.2.6}$$

$$\Delta t_{cool,2}(t) = \frac{\mu}{\gamma+1}\frac{k_B T_{RS}}{\rho_{ej}(R_{RS},t)\,\Lambda(T_{RS})}. \tag{5.2.7}$$

In these equations, ρ_0 and $\rho_{ej}(R_{RS},t)$ are the density of the ambient gas and that

of the unshocked ejecta, respectively. Λ is the cooling function introduced in chapter 4 and T_{LS} and T_{RS} are the temperatures behind the leading and the reverse shocks, respectively.

The cooling rate in the outer shell is:

$$Q_1 = \sum_{i,j} n^2_{shell,i,j} \Lambda \left(T_{LS}\right) \Omega_{i,j}, \tag{5.2.8}$$

where $n_{shell,i,j}$ and $\Omega_{i,j}$ are calculated by means of equations 4.4.4 and 4.4.5, respectively.

The cooling rate behind the reverse shock is:

$$Q_2 = \bar{n}^2 \Lambda \left(T_{RS}\right) \Omega_2, \tag{5.2.9}$$

where:

$$\bar{n} = \frac{P_{RS}}{k_B T_{RS} m_H}, \tag{5.2.10}$$

$$\Omega_2 = \frac{M_{th}}{\bar{\rho}}, \quad \bar{\rho} = \mu m_H \bar{n}. \tag{5.2.11}$$

In these equations, M_{th} is the ejecta mass that passed through the reverse shock (calculated from equation 3.3.3) and P_{RS} is the pressure behind the reverse shock (calculated from equation 3.5.3).

Results

SNR evolution in a low density ambient medium

As a test case, a complete evolution of an SNR in a low density ambient medium ($n_0 = 1$ cm^{-3}) was calculated.

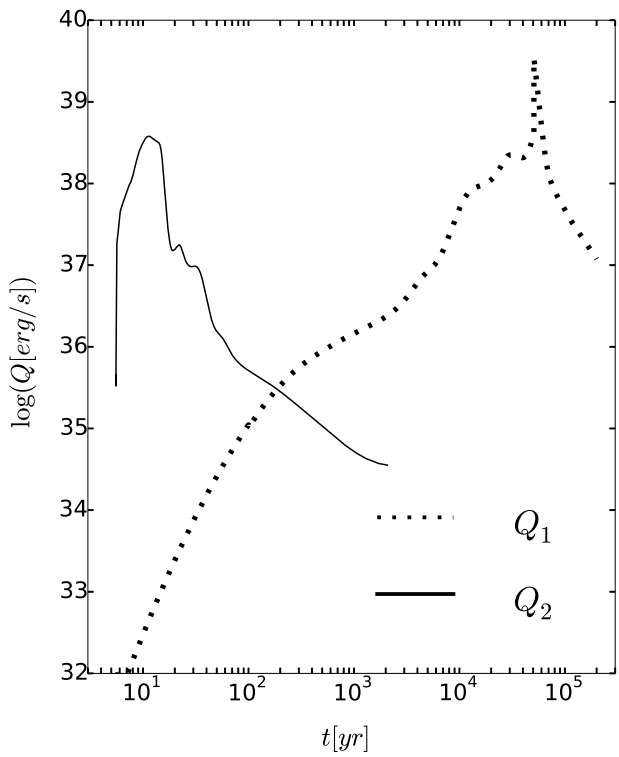

Figure 5.1: *Rate of energy loss from the outer (dotted) and inner shells (solid) for the case of* $n_0 = 1\ cm^{-3}$.

The radiative losses of energy from the reverse (Q_2) and leading (Q_1) shocks are shown in Fig. 5.1. One can notice a short period, $\Delta t \approx 20$ yr, when strong radiative cooling from an initially weak reverse shock dominates. During this time, the fraction of ejecta mass cooled by radiation is:

$$M_{ej}^{rad} = 0.014 M_{ej}. \tag{5.3.1}$$

These values of Δt and M_{ej}^{rad} are in good agreement with the results presented in Truelove & McKee (1999).

Fig. 5.1 shows that during most part of the evolution, Q_2 is small compared to Q_1. Note that the peak of Q_1 occurs around the transition time to the Snowplough (SP)

stage. This is in agreement with previous results, as sometimes the peak of luminosity has been used in order to estimate the characteristic time to the Snowplough transition (Thornton et al., 1998).

The full evolution of thermal, kinetic and total energies is shown in Fig. 5.2. The transition time from the ST to the SP stage occurs about $t \approx 5 \times 10^4\ yr$ and agrees with that obtained in the previous chapter. Note also that during the last stages $E_{tot} \approx E_{k,ism}$.

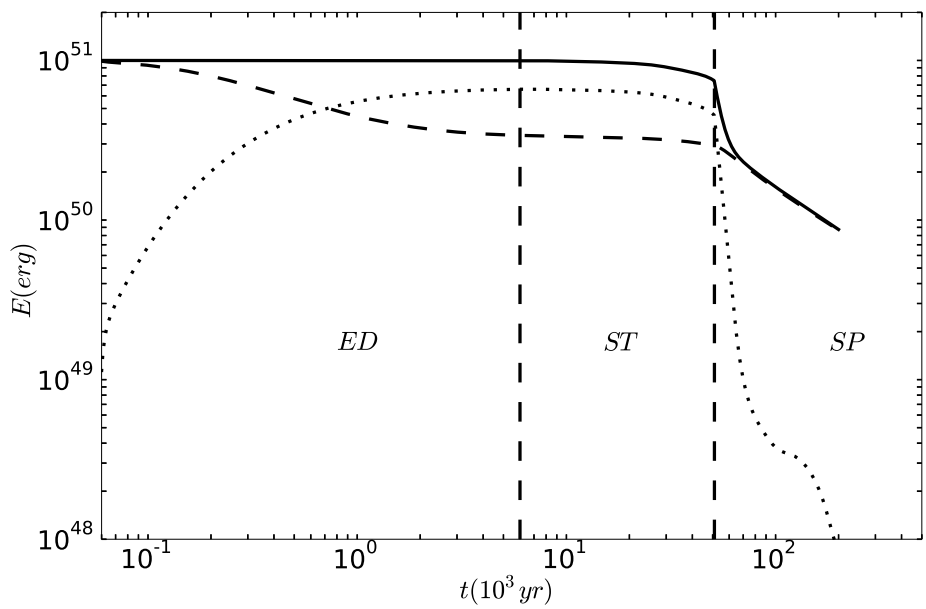

Figure 5.2: *Evolution of the total, thermal and kinetic energies (solid, dotted and dashed lines, respectively) for a SNR evolving in the ambient medium with density $n = 1\ cm^{-3}$. The three evolutionary stages are marked by the vertical lines.*

SNR evolution in a high density medium

A test case for SNR evolution in a high density ISM was presented in Terlevich et al. (1992), who selected a density of $n_0 = 10^7\ \mathrm{cm}^{-3}$ for the ambient gas.

To compare our simulations with these results, the structure and velocity of the

ejecta and the initial conditions discussed in the previous chapters were modified (see Appendix C).

The early (first 10 yr) evolution of the reverse and the leading shock radii in this case is presented in Fig. 5.3. One can note that the evolution proceeds very rapidly and that in this case the distance between the leading and the reverse shock is small due to strong radiative cooling.

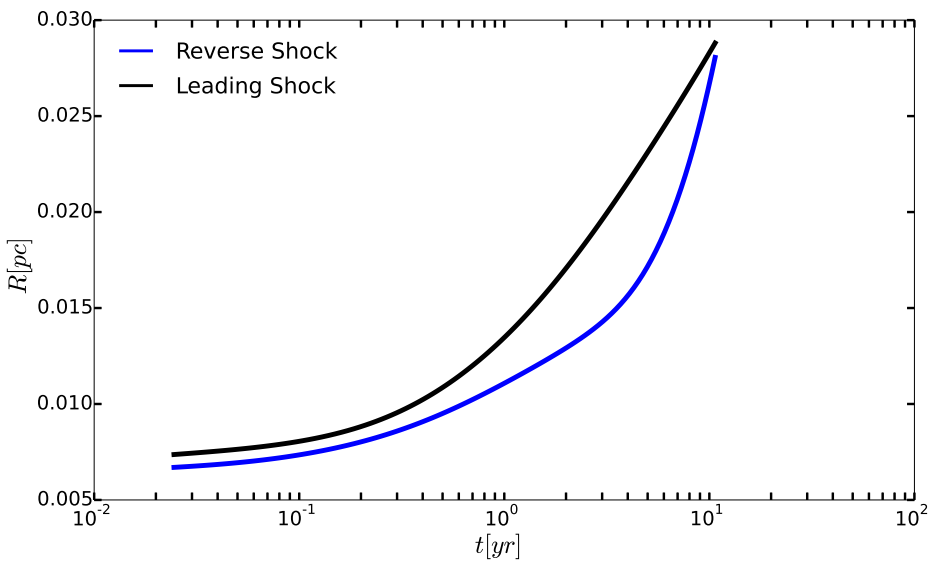

Figure 5.3: *The reverse and leading shock positions for a SNR evolving into an ambient medium with density* $n = 10^7\ cm^{-3}$.

One can compare the results of our simulations presented in Fig. 5.3 with the results obtained by Terlevich et al. (1992) at two evolutionary times ($t = 0.53$ yr and $t = 4.5$ yr). Table 5.1 presents the calculated values of R_{LS} and R_{RS} and compares them to those of Terlevich et al. (1992) (shown in parenthesis). The leading and the reverse shock radii obtained in the 2D numerical simulation and in the Thin-Shell approximation are in good agreement.

Table 5.1: The leading and the reverse shock positions obtained in our calculation and in Terlevich et al. (1992); in parenthesis, at two different stages.

R	$t = 0.53\ yr$	$t = 4.5\ yr$
$R_{LS}[10^{-2}pc]$	1.10(1.08)	2.20 (2.15)
$R_{RS}[10^{-2}pc]$	0.96(0.84)	1.50 (1.52)

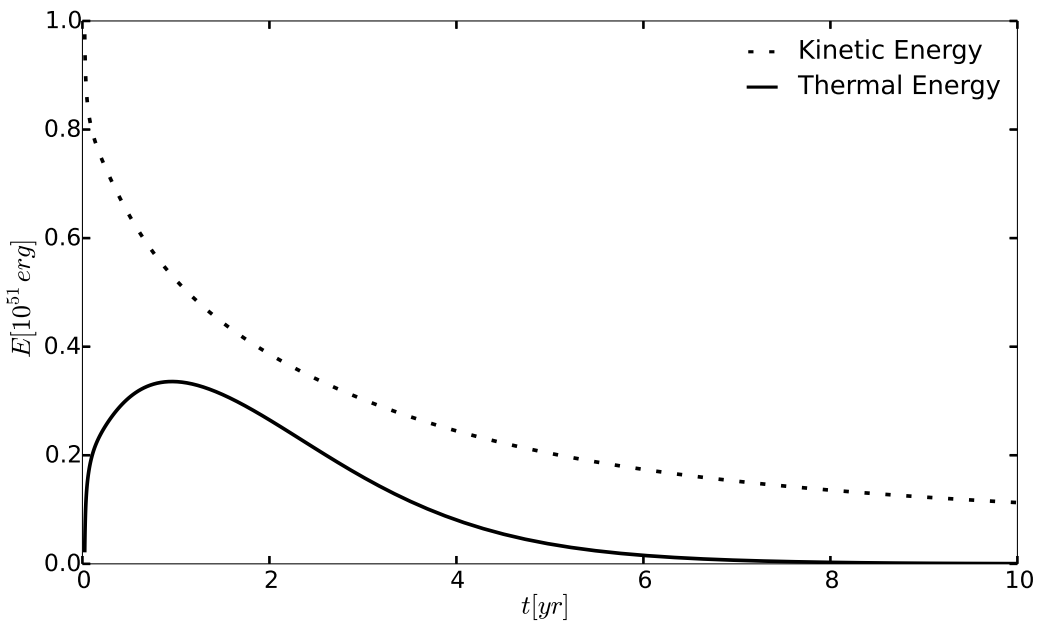

Figure 5.4: *The kinetic (dotted line) and thermal (solid line) energies of the SNR evolving in an ambient medium with density* $n = 10^7 cm^{-3}$.

Fig. 5.4 presents the evolution of the remnant energies. As one can note, strong radiative cooling leads to a considerable decrease of the thermal energy in a short time interval and it never reaches $E_{th} = 0.66E_0$. Therefore the Sedov-Taylor stage is completely inhibited. Our results are in excellent agreement with those presented in Fig. 1 of Terlevich et al. (1992).

Fig. 5.5 presents the evolution of the ejecta and swept-up gas energies in the high density calculation. The panel (a) shows how the kinetic energy of the shocked ambient medium rapidly grows to values expected for the ST stage, however, the lost of thermal pressure yields to a faster deceleration of the outer shell and therefore to a rapid decrease of its kinetic energy. The panel (c) shows that the kinetic energy of the shocked ejecta remains small during the entire evolution. This is because strong radiative cooling makes the reverse shock less strong and hence, the rate at which the ejected mass passes through it is smaller in the high density cases. This figure also shows that at late times the kinetic energy of the outer expanding shell (panel a) dominates over the total thermal energy (panel d) and kinetic energies of the ejecta (panels b and c).

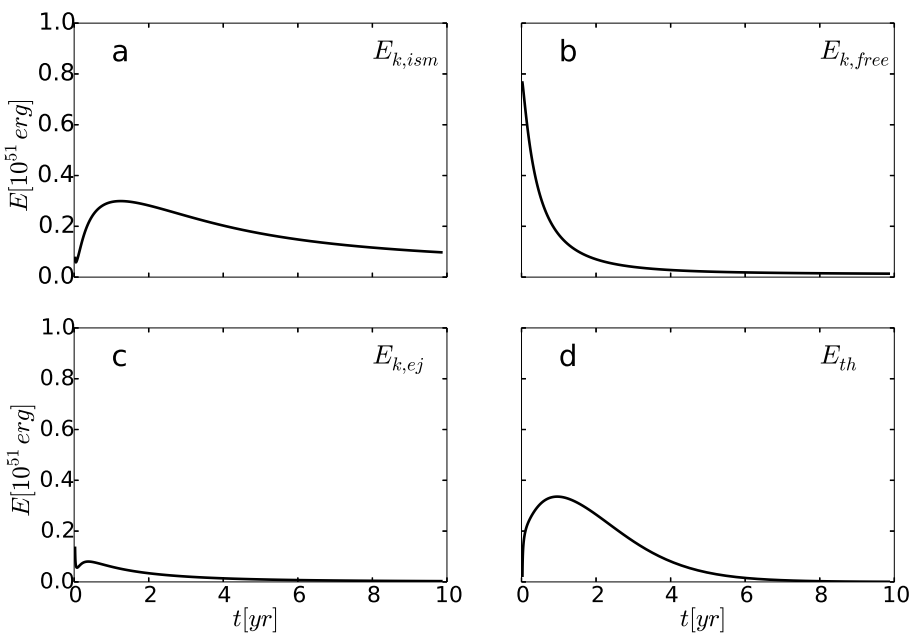

Figure 5.5: *Evolution of the SNR energy in the case of a high density ($n_0 = 10^7\ cm^{-3}$) ambient medium. $E_{k,ism}$, $E_{k,free}$, $E_{k,ej}$ are the kinetic energies of the shocked ambient gas, the free ejecta, and the shocked ejecta, respectively. E_{th} is the thermal energy.*

The trace of the ejecta structure on the SNRs dynamics at high density

Fig. 5.6 presents the evolution of the remnant energies for an ejecta structure given by power-law functions with indexes $n = 0$ and $n = 2$ (as in chapter 3). The SN is assumed to explode in an ambient medium of density $n_0 = 10^7$ cm^{-3}. The evolution depends on the ejecta structure. All the remnant energies on Fig. 5.6 differs from the ones presented in the Fig. 5.5. For instance, the thermal energy reaches different peaks for the three possibilities of the ejecta density considered in this work.

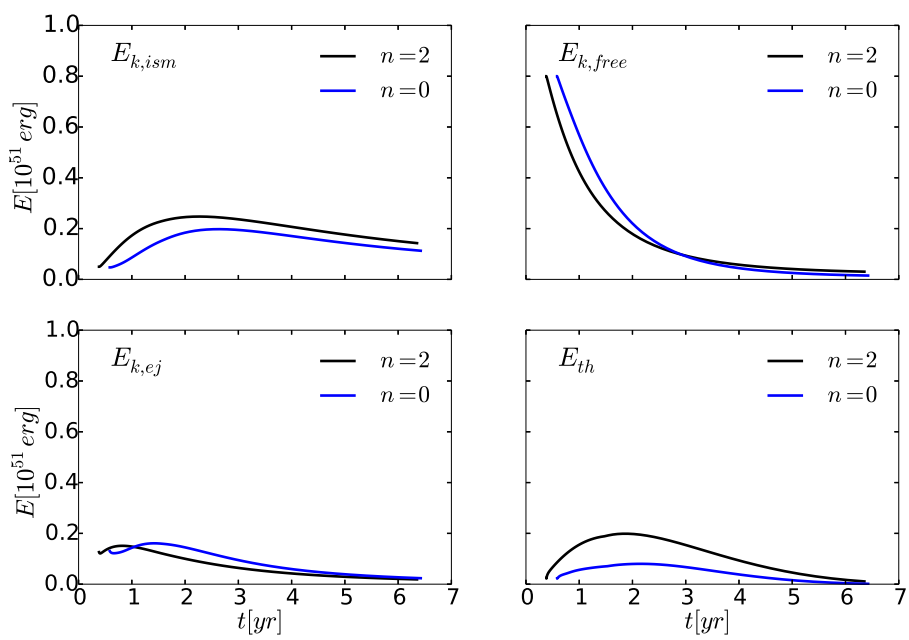

Figure 5.6: *Evolution of the kinetic energies $E_{k,ism}$, $E_{k,free}$, $E_{k,ej}$, and the thermal energy E_{th} of a remnant evolving into an ambient medium of density $n_0 = 10^7$ cm^{-3}, for two different ejecta densities: $n = 0$ and $n = 2$ (see chapter 3.1).*

In all the cases, however, the reverse shock is not able to move rapidly into the expanding ejecta, as the thermal energy and therefore the thermal pressure decreases

behind both shocks. Hence, in a short period of time ($t \approx 6 - 11$ yr), the shocked ambient gas and the shocked ejecta merge to form a dense shell, see also Terlevich et al. (1992). The further evolution of the remnant at such cases is addressed in section 5.6. For the remaining part of this chapter, the calculations are performed assuming a power-law $n = 2$ for the ejecta density.

The Thermalization of the ejecta mass

SNRs do not enter the Sedov-Taylor stage if the density of the ambient medium is $n_0 = 10^7$ cm^{-3}, because in this case radiative cooling is very strong even at the ED stage. The numerical approximation developed in this work allows one to study the evolution of SNRs considering a wide range of values for the ambient density. This is a difficult task for full hydrodynamical codes, because a high spatial and temporal resolutions are required in order to follow correctly the evolution of compact radiative shells.

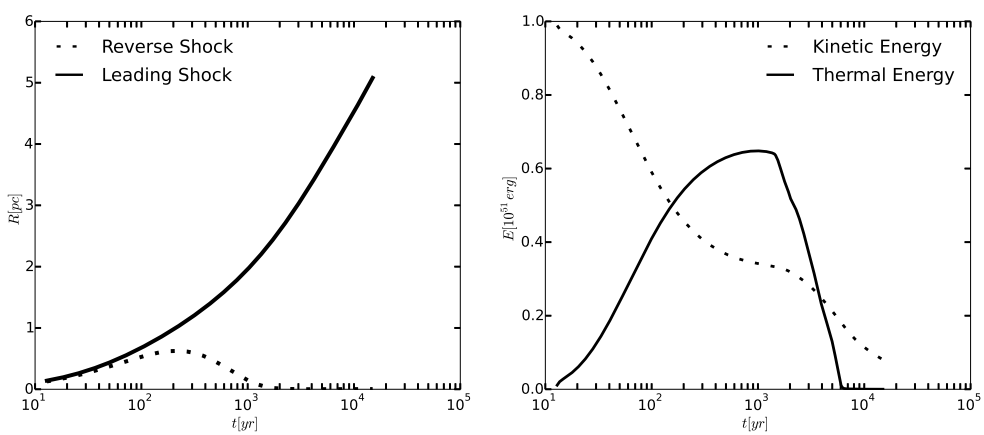

Figure 5.7: *The shock positions and energies evolution for a SNR evolving into an ambient medium of density* $n_0 = 10^2$ *cm*$^{-3}$.

Our aim in this section is to study the impact of the ambient density n_0 on the early evolution of SNRs, i.e, for the ejecta-dominated stage. Simulations were carried out for densities n_0 [cm^{-3}] = 10^2, 10^3, 5×10^3, 10^4, 5×10^4, 10^5, 10^6, 10^7. A $M_{ej} = 3$ M$_\odot$ ejecta with initial kinetic energy $E_0 = 10^{51}$ erg and a power-law index $n = 2$ for the ejecta density have been used in these calculations.

Fig. 5.7 presents the results for the $n_0 = 10^2$ cm^{-3} model. One can note that the remnant follows the usual evolutionary track. All the ejecta mass is thermalized at the age of $t \approx 1115$ yr. At this time, the ratio of the ambient swept up mass to the ejecta mass is about 38, which is in agreement with the results of Gull (1973) and Tenorio-Tagle et al. (1990). The time of the cold thin-shell formation t_{sf} for the leading shock, i.e the transition to the Snowplough stage, is about 3216 yr after the explosion (see the right panel of Fig. 5.7).

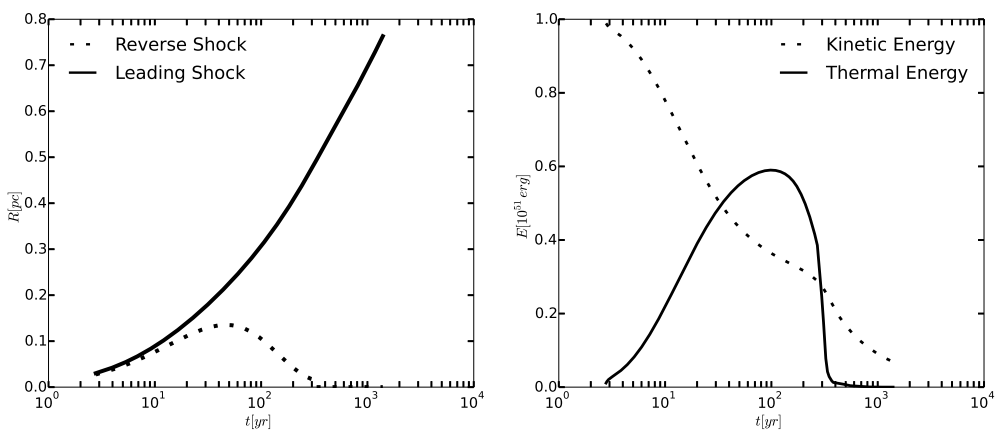

Figure 5.8: *Same as Fig. 5.7 but for* $n_0 = 10^4$ *cm*$^{-3}$.

For larger ambient gas densities, cooling becomes important even earlier. For example, the results of our simulation in the case $n_0 = 10^4$ cm^{-3} are presented in Fig. 5.8. In this case, the thermalization of the ejecta culminates at about 250 yr and the remnant reaches the Snowplough stage at the time $t \approx 270$ yr without having reached the ST phase. For higher densities, the remnant enters the Snowplough stage

earlier, when the ejecta has not even been completely thermalized.

Table 5.2 summarizes the results of the calculations for all the cases. the shell formation time t_{sf} is shown in the second column. At this time strong radiative cooling sets in and the SNR evolves into the Snowplough stage. The mass of the thermalized ejecta at this time $M_{th,ej}(t_{sf})$ is shown in the third column. If $M_{th,ej}(t_{sf})$ is less than the total ejecta mass, the remnants enter the strong radiative cooling phase before ending the thermalization process. Hence, such remnants do not evolve into the ST stage.

Table 5.2: Properties of SNRs evolving into different ambient media. The second column is the shell formation time t_{sf} (see text) and the third column shows the mass of the thermalized ejecta measured at t_{sf}.

n_0 [cm^{-3}]	t_{sf} [yr]	$M_{th,ej}(t_{sf})$ [M$_{ej}$]
10^2	3215.7	1.0
10^3	1054.5	1.0
5×10^3	404.7	1.0
10^4	271.2	1.0
5×10^4	100.4	0.97
10^5	60.4	0.93
10^6	10.2	0.70
10^7	1.19	0.29

Table 5.2 shows that for the adopted model of the ejecta, the remnant enters the Snowplough stage after the thermalization of the ejecta only for densities lower than $n_{cri} = 10^4$ cm^{-3}. For densities $n > n_{cri}$, the remnant becomes radiative when the fraction of unshocked ejecta is still non-negligible and therefore the kinetic and thermal energies of the remnant do not reach the ST values.

Even in the models with $n < n_{cri}$, SNRs do not evolve exactly as the ST solution predicts. Indeed, as the cooling rate depends on the shocked ambient gas density, only in the case of the lowest densities the energy lost by radiation is small enough to permit the remnant to reach the ST stage with the predicted value of thermal

energy ($E_{th} \approx 0.66E_0$, see chapter 2). Fig. 5.9 shows the thermal energies of SNRs evolving in ambient media with different densities. Note that only for $n_0 < 10^2$ cm^{-3}, the thermal energy approaches the ST value.

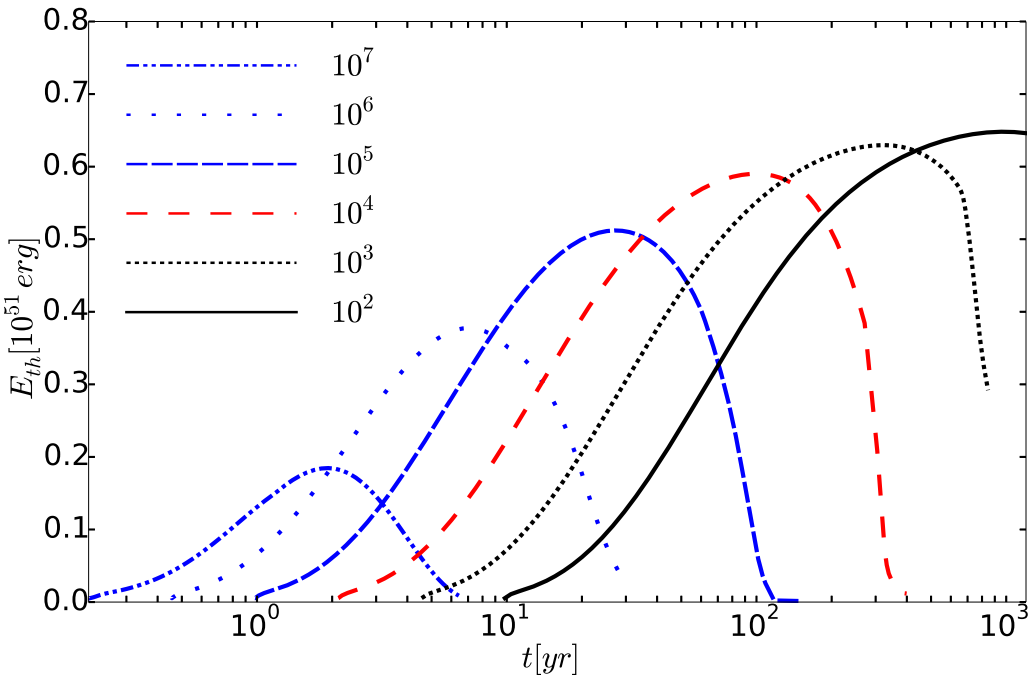

Figure 5.9: *The thermal energy for a SNR evolving into an ISM with different densities.*

The full evolution of SNRs in high density media

Section 5.4 discussed how the rapid decrease of the thermal pressure leads to the merging of the shells of shocked ejecta and shocked ambient gas into a very thin and dense expanding shell. At this time the free ejecta gas still moves with a large velocity ($v_{ej} \approx 10^3$ km s^{-1}) and cools effectively. This shell keeps sweeping up the ambient gas and is pushed by the ram pressure of the ejecta P_{ram}. At the same time, the shell also incorporates a fraction of the ejecta mass as it rapidly decelerates.

The equations governing such shell dynamics are the mass and momentum conservation equations:

$$\frac{dM_{shell}}{dt} = 4\pi R_{shell}^2 \left(\rho_0 U_{shell} + \rho_{ej}\left(R_{shell}, t\right) \left[\frac{R_{shell}}{t} - U_{shell} \right] \right), \tag{5.6.1}$$

$$M_{shell}\frac{dU_{shell}}{dt} = 4\pi R_{shell}^2 P_{ram} - U_{shell}\frac{dM_{shell}}{dt}, \tag{5.6.2}$$

$$\frac{dR_{shell}}{dt} = U_{shell}. \tag{5.6.3}$$

In these equations, M_{shell}, R_{shell} and U_{shell} are the shell mass, position and velocity, respectively. The first term in equation 5.6.1 takes into account the mass of swept up ambient gas and the second term the mass of shocked ejecta. These equations are solved taking as initial conditions the values of mass, radius and velocity of the remnant at the moment when the shells merge.

Fig. 5.10 shows the shell radius after the shells merge by a dashed line. In this case, the merging occurs at about 8 yr after the explosion.

The shell stalls at about $t_{stall} = 220$ yr because at that time the ram pressure of the ejecta drops below the ambient pressure[1] P_{amb}, i.e., $P_{ram} < P_{amb}$ (see Fig. 5.11). At this time, the radius of the shell is $R_{stall} \approx 0.058$ pc and its mass is $M_{shell} = 258$ $M_\odot$, which contains about 2.94 $M_\odot$ from the ejecta. Therefore, at the stalling point, about 3% of the ejecta gas has not yet been shocked.

[1] P_{amb} is calculated assuming a temperature $T_{amb} = 1000$ K.

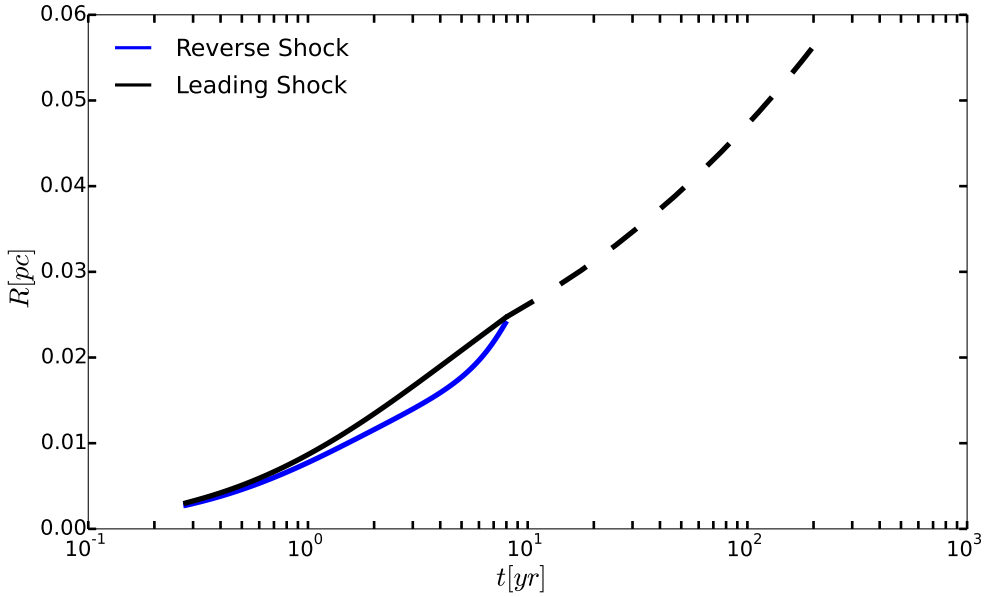

Figure 5.10: *The reverse and leading shock positions for a remnant evolving into an ambient medium of density* $n_0 = 10^7$ *cm*$^{-3}$*. The dashed line indicates the evolution of the expanding shell formed at the outer boundary.*

Conclusions

This chapter has presented a method that allowed us to simulate the full evolution of SNRs into different ambient media. For the low density cases, our results are in agreement with previous results and a briefly early radiative period for the shocked ejecta gas was found. The high density cases were successfully tested with a density $n_0 = 10^7$ cm^{-3}. Simulations were performed over a wide range of densities in order to study the impact of radiative cooling on the evolution of SNRs. The critical density that allows a remnant to thermalize its ejected mass before the onset of the strong radiative phase is found. Finally, the fate of remnants evolving into an ambient medium of density $n_0 = 10^7$ cm^{-3} is addressed.

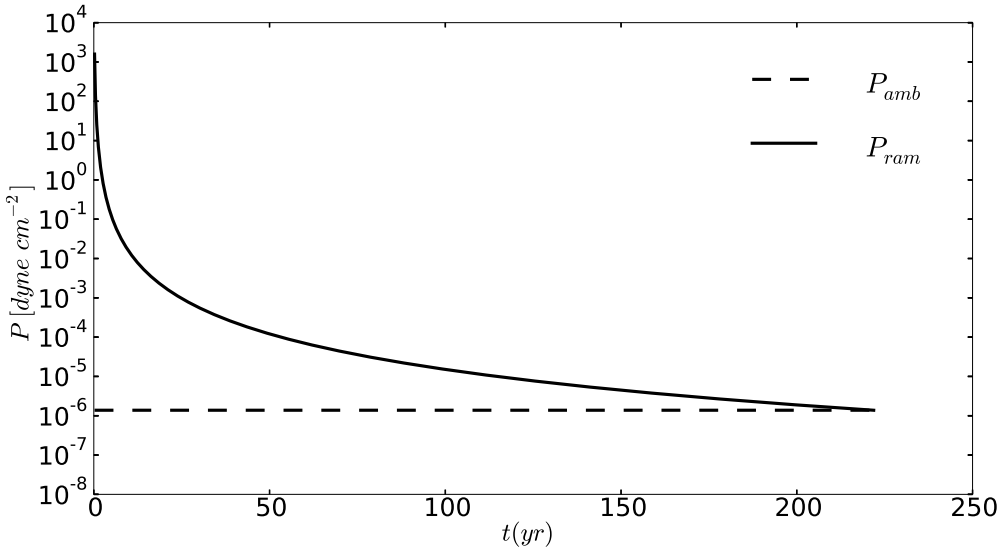

Figure 5.11: *Evolution of the ejecta ram pressure P_{ram} (solid line) for a SNR evolving into an ambient medium of density $n_0 = 10^7\ cm^{-3}$ and temperature $T_{amb} = 1000\ K$. The dashed line shows the ambient pressure.*

Chapter 6
Concluding Remarks

The aim of this Thesis is to study the full evolution of SNRs, from the ejecta-dominated to the Snowplough stage. For this purpose, a 3D numerical scheme based on the Thin-Shell approximation was developed. This numerical scheme accounts for the ejecta structure and strong radiative cooling and allows one to study the SNRs evolution in a wide range of circumstances efficiently.

Such studies are of paramount importance in the understanding of supernova explosions and their remnants evolution in a number of cases where their feedback is considered to be important (e.g. star clusters, galaxies and star-forming clouds).

The main conclusions derived from this work are:

- The Thin-Shell code has reproduced with high accuracy the Sedov-Taylor solution, both the kinetic and thermal energy fractions as well as the leading shock position and expansion velocity. Although it was not the main goal of this work, the evolution of a SNR in a non-homogeneous ISM could also be simulated by making use of this code.

- The ejecta-dominated phase was studied for several ejecta models. The initial condition of the ejecta mass distribution was shown to have imperceptible consequences on the long-term evolution of SNRs in low-density cases.

- The transition time from the Sedov-Taylor to the Snowplough phase was defined, calculated and compared with previous results. A good agreement between ours and other groups calculations was obtained in all cases. The leading

shock position was found to change as $R \propto t^{0.4}$ during the Sedov-Taylor stage and as $R \propto t^{0.3}$ during the Snowplough phase.

- In models with low ambient density, the energy radiated by the shocked ejecta is important only for an initial short period of time. For most part of the evolution, the reverse shock can be considered as an adiabatic shock. The peak of the rate of energy loss of the shocked ambient gas was found to be very near to the transition time to the Snowplough stage.

- Our results for a SN explosion in a high density medium of $n_0 = 10^7$ cm^{-3} are in excellent agreement with the results presented in Terlevich et al. (1992). In such case, radiative cooling of the swept-up ambient gas and of the shocked ejecta is important very early in the SNR evolution. The remnant loses most of its thermal energy approximately 10 yr after the explosion.

- It was shown that the ejecta density structure does change the evolution of SNRs for the $n_0 = 10^7$ cm^{-3} model. However, in all cases, strong radiative cooling leads to a rapid decrease of the thermal energy and to the formation of a dense, cold expanding shell, pushed by the unshocked ejecta ram pressure. The shell continues its expansion while sweeping-up ambient gas and collecting the ejecta until the ram pressure is comparable to the ambient pressure. At this point, the shell stalls and merges with the ambient medium.

- Simulations were carried out for densities ranging from $n_0 = 1$ up to $n_0 = 10^7$ cm^{-3}. A critical density $n_{cri} = 10^4$ cm^{-3} was determined. The SNRs manage to thermalize all the ejected mass before the onset of the Snowplough stage if $n_0 < n_{cri}$. Otherwise, a non-negligible part of the ejecta mass has yet to be shocked by the time the remnant becomes fully radiative without reaching the ST phase.

Future work

The model here discussed can be extended to include the radiation from dust particles. It is important to integrate all the relevant processes as SNRs have been identified

as major producers of interstellar dust (e.g.Morgan et al. 2003, Dunne et al. 2003, Maiolino et al. 2004) and the cooling by dust can be up to two orders of magnitude more effective than gas cooling, impacting noticeably the hydrodynamical evolution of such remnants and the feedback they provide to the environment (e.g. Tenorio-Tagle et al. 2013, Martínez-González et al. 2016).

It would also be interesting to study how the results of this work can contribute to the understanding of dust formation during the early life of the Universe. Low-mass evolved stars cannot be a source of dust formation at these ages, because their evolutionary time scale are longer than the age of the universe at that moment. Therefore, it is expected that most of the dust grains formed in the supernova ejecta (e.g.Todini & Ferrara 2001, Marchenko 2006, Bianchi & Schneider 2007b). However, although a non-negligible amount of dust is formed in the cold ejecta, just a small fraction (about $10 - 20\%$) survives the passage through the reverse shock (e.g. Micelotta et al. 2016, Hwang & Laming 2012).

Our results show that the reverse shock is much weaker for SNRs evolving into high density media, therefore, it is expected that a larger fraction of dust grains could survive in these cases. At the same time, the high densities and low temperatures of the shells are likely to enhance the formation of dust grains. Both effects can lead to explain the reason to observe high redshift objects with such a large amount of dust (Hines et al., 2006).

Appendices

Appendix

The pressure ratio at the beginning of the ED and at the ST stages

Here, the pressure ratio ϕ (see chapter 3) is estimated at the early ejecta-dominated phase and during the Sedov-Taylor stage. It is shown that in both cases ϕ is close to 0.3.

The ejecta-dominated phase

At the ED stage, the pressure gradient between the leading shock P_{LS} and the reverse shock P_{RS} can be estimated from the stationary Euler equation:

$$\frac{dP}{dr} = -\rho u \frac{du}{dr}. \tag{A.1.1}$$

At the initial time t_0:

$$P_{RS} - P_{LS} \approx -\rho_{LS} U_{LS} \left(U_{RS} - U_{LS} \right), \tag{A.1.2}$$

where ρ_{LS} is the density behind the leading shock, U_{LS} and U_{RS} are the gas velocities behind the leading and the reverse shock in the rest frame, respectively. The ratio of the gas pressures ϕ then is:

$$\phi = \frac{P_{RS}}{P_{LS}} = 1 - \frac{\rho_{LS} U_{LS}}{P_{LS}} \left(U_{RS} - U_{LS} \right). \tag{A.1.3}$$

From the Rankine-Hugoniot conditions

$$P_{LS} = \frac{\gamma+1}{2}\rho_0 U_{LS}^2, \quad \rho_{LS} = \frac{\gamma+1}{\gamma-1}\rho_0, \tag{A.1.4}$$

where ρ_0 is the density of the ambient medium. Substituting A.1.4 into A.1.3 one can obtain:

$$\phi = 1 - \frac{2}{\gamma-1}\left(\frac{U_{RS}}{U_{LS}} - 1\right). \tag{A.1.5}$$

The post-shock velocities are:

$$U_{RS} = \frac{2}{\gamma+1}V_{RS} + \frac{\gamma-1}{\gamma+1}\frac{R_{RS}}{t}, \tag{A.1.6}$$

where V_{RS} and R_{RS} are the velocity and position of the reverse shock and γ is the specific heats ratio. At t_0:

$$V_{RS}(t_0) = \frac{R_{RS}(t_0)}{t_0} = V_{max}, \tag{A.1.7}$$

where V_{max} is the maximum velocity of the free ejecta at the initial time. Therefore:

$$U_{RS}(t_0) = V_{max}. \tag{A.1.8}$$

The gas velocity behind the leading shock U_{LS} is (see chapter 3):

$$U_{LS}(t_0) = \frac{2}{\gamma+1}l_{ED}V_{max}, \tag{A.1.9}$$

where $l_{ED} = 1.1$ is the leading factor (see chapter 3). Substituting equations A.1.8 and A.1.9 into equation A.1.5, one can obtain:

$$\phi(t_0) = 1 - \frac{2}{\gamma-1}\left(\frac{\gamma+1}{2l_{ED}} - 1\right) = 0.3636. \tag{A.1.10}$$

The Pressure ratio in the Sedov-Taylor solution

During the Sedov-Taylor (ST) stage, the reverse shock has already reached the center of the explosion, therefore ϕ is equivalent to the ratio between the central gas pressure P_c and the pressure behind the leading shock: P_c/P_{LS}. It was calculated as a function of the specific heats γ by Gaffet (1978):

$$\phi = 1 - \frac{1}{\omega_s\left(1+2\omega_s\right)}\left(q_1 + \frac{2\omega_s\left(1-\omega_s\right)X_0}{2+\omega_s}\right), \tag{A.2.1}$$

where:

$$\omega_s = \frac{2}{1+\gamma}, \tag{A.2.2}$$

$$X_0 = \left(2-\omega_s\right)\left(2+5\omega_s-4\omega_s^2\right) + q_0\left(5\omega_s^2-2\omega_s-11\right) + q_0^2\left(5-\frac{3}{2}\omega_s\right). \tag{A.2.3}$$

$$\frac{q_1}{\omega_s\left(1-\omega_s\right)} = \left(\frac{4-3\omega_s}{1-\omega_s}\right)q_0 - 2\left(2-\omega_s\right), \quad \text{if } \gamma \neq 1, \tag{A.2.4}$$

and

$$q_0 = -\frac{R_{LS}\frac{dU_{LS}}{dt}}{U_{LS}^2} = 3/2. \tag{A.2.5}$$

For $\gamma = 5/3$, equation A.2.1 gives $\phi \approx 0.3045$.

Appendix

Analytic expressions for the reverse and the leading shocks

The analytic expressions for the leading and reverse shock radii and velocities are presented in (Truelove & McKee, 1999, hereafter TM99), who used:

$$M_{ch} = M_{ej}, \tag{B.0.1}$$

$$R_{ch} = M_{ej}^{1/3} \rho_0^{-1/3}, \tag{B.0.2}$$

$$t_{ch} = E^{-1/2} M_{ej}^{5/6} \rho_0^{-1/3}, \tag{B.0.3}$$

as units of mass, radius and time. In these units, a non-dimensional form of any physical variable x is:

$$x^* = x / R_{ch}^{\beta 1} t_{ch}^{\beta 2} M_{ch}^{\beta 3}, \tag{B.0.4}$$

where β_1, β_2 and β_3 are constants. M_{ej}, E and ρ_0 are the ejecta mass, the explosion energy and the ambient medium density, respectively. Note that the TM99 solution is adiabatic and thus does not take into account the effects of radiative cooling.

The ejecta-dominated phase

In the TM99 solution the position of the leading shock R_{LS}^* during the ED-phase is given implicitly as a function of time:

$$t^* \left(R_{LS}^*\right) = 0.6428 \left(\frac{3-n}{5-n}\right)^{1/2} R_{LS}^* \left[1 - 0.3493 \left(3-n\right)^{1/2} R_{LS}^{*3/2}\right]^{-\frac{2}{3-n}}. \tag{B.1.1}$$

The leading shock velocity V^*_{LS} as a function of R^*_{LS} is:

$$V^*_{LS} = 1.556 \left(\frac{5-n}{3-n}\right)^{1/2} \frac{\left[1 - 0.34926\,(3-n)^{1/2}\, R^{*3/2}_{LS}\right]^{\frac{5-n}{3-n}}}{1 + 0.34926 R^{*3/2}_{LS} \frac{n}{(3-n)^{1/2}}}. \tag{B.1.2}$$

The reverse shock position and velocity are:

$$t^*\left(R^*_{RS}\right) = 0.7071 \left(\frac{3-n}{5-n}\right)^{1/2} R^*_{RS} \left[1 - 0.7612\,(3-n)^{1/2}\, R^{*3/2}_{RS}\right]^{-\frac{2}{3-n}}, \tag{B.1.3}$$

$$V^*_{RS}\left(R^*_{RS}\right) = 3.2296 \frac{(5-n)^{1/2}}{3-n} R^{*3/2}_{RS} \frac{\left[1 - 0.7612\,(3-n)^{1/2}\, R^{*3/2}_{RS}\right]^{\frac{2}{3-n}}}{1 + 0.7612 R^{*3/2}_{RS} \frac{n}{(3-n)^{1/2}}}. \tag{B.1.4}$$

The Sedov-Taylor Stage

During the ST phase, the shock positions and velocities are:

$$R^*_{LS}\left(t^*\right) = \left[0.4506 + 1.4233 \left(t^* - 0.6390 \left(\frac{3-n}{5-n}\right)^{1/2}\right)\right]^{2/5}, \tag{B.2.1}$$

$$V^*_{LS}\left(t^*\right) = 0.5694 \left[0.4506 + 1.4233 \left(t^* - 0.6390 \left(\frac{3-n}{5-n}\right)^{1/2}\right)\right]^{-3/5}, \tag{B.2.2}$$

$$\begin{aligned} &R^*_{RS}\left(t^*\right) \\ &= t^* \left[1.1 - (0.106 - 0.128n) \left(t^* - 0.6390 \left(\frac{3-n}{5-n}\right)^{1/2}\right)\right. \\ &\quad \left. - \left(0.585 - 0.6390\,(0.106 - 0.128n) \left(\frac{3-n}{5-n}\right)^{1/2}\right) \ln\left(1.5649 \left(\frac{5-n}{3-n}\right)^{1/2} t^*\right)\right], \end{aligned} \tag{B.2.3}$$

$$V^*_{RS}\left(t^*\right) = \frac{R^*_{RS}}{t^*} - \left[0.585 + (0.106 - 0.128n) \left(t^* - 0.639 \left(\frac{3-n}{5-n}\right)^{1/1}\right)\right]. \tag{B.2.4}$$

The transition time between the ED and SR stages is:

$$t^*_{ST} = 0.495 \left[\frac{5}{3} \left(\frac{3-n}{5-n} \right) \right]^{1/2} . \tag{B.2.5}$$

Appendix

Initial conditions for high density runs

The ejecta density profile and its velocity structure in the pioneer hydrodynamical simulations presented at Terlevich et al. (1992) and related works (e.g, Franco et al. 1991; Tenorio-Tagle et al. 1991) are here discussed. A method to introduce this prescription for the ejecta structure within the frame of chapter 3 is also addressed.

The density and velocity structure

A power-law density $\rho_{ej} \propto r^{-n}$ for the ejecta gas was assumed throughout this work (see chapter 3). It was also assumed that $n < 3$ and therefore an ejecta core was not needed. Now, the following structure is considered:

$$v\left(r,t\right) = \begin{cases} \frac{r-R_c}{R_{ej}(t)-R_c} & \text{if } r \geq R_c, \\ 0 & \text{if } r < R_c, \end{cases} \tag{C.1.1}$$

where:

$$R_{ej}\left(t\right) = R_{ej}^0 + v_{ej}t, \tag{C.1.2}$$

is the free-expansion radius of the ejecta, v_{ej} is the ejecta maximum velocity and R_c is the inner surface of the ejected mass, i.e., the boundary defining the size of the stellar remnant. The term R_{ej}^0 is the initial outer boundary of the ejected matter. The mass

M_{ej} expelled by the explosion is assumed to be located between R_c and $R_{ej}(t)$:

$$\rho_{ej}(r,t) = \begin{cases} \frac{M_{ej}}{4\pi \ln(R_{ej}(t)/R_c)} r^{-3} & \text{if } r \geq R_c, \\ 0 & \text{if } r < R_c, \end{cases} \tag{C.1.3}$$

Equations C.1.2 and C.1.3 yield the following equation for the kinetic energy of the free ejecta:

$$E_{k,free}(r,t) = \frac{M_{ej} v_{ej}^2}{2\ln(R_{ej}(t)/Rc)(R_{ej}(t) - R_c)^2} \left[\frac{1}{2}\left(r^2 - R_c^2\right) - 2R_c(r - R_c) + R_c^2 \ln(r/R_c) \right] \tag{C.1.4}$$

The kinetic energy of the shocked ejecta $E_{k,ej}$ is still calculated as in chapter 3 (see equation 3.3.2), the only difference is that the fraction of M_{ej} that has been shocked by the reverse shock is now given by:

$$M_{th} = M_{ej}(1 - \frac{\ln(R_{RS}/R_c)}{\ln(R_{ej}(t)/R_c)}) \tag{C.1.5}$$

Te introduction of equations C.1.4 and C.1.5 into the Thin-shell code require the knowledge of R_c and R_{ej}^0, as also of E_0 , M_{ej} and v_{ej}. This is possible by setting the initial configuration of the explosion at time $t = 0$, as discussed in the next section.

Initial condition at $t = 0$

At $t = 0$, the leading shock is assumed to be at R_{ej}^0 and therefore the total explosion energy E_0 is the kinetic energy of the free ejecta, which is located between R_c and R_{ej}^0. Hence, at $t = 0$:

$$E_{k,free}(t=0) = E_0 = \frac{M_{ej} v_{ej}^2}{4\ln(x)(1-x)^2}\left[x^2 - 4x + 3 + 2\ln(x)\right], \tag{C.2.1}$$

where

$$R_{ej}^0 = xR_c. \tag{C.2.2}$$

Equation C.2.1 is a non-linear equation in x that can be solved if values of M_{ej}, E_0 and v_{ej} are given.

The density at the outer boundary R^0_{ej} is assumed to be equal to ρ_0, the density of the ambient medium (Rodríguez-González, 2000):

$$\rho_{ej}\left(R^0_{ej}, t = 0\right) = \rho_0. \tag{C.2.3}$$

Equation C.2.3 allows one to calculate R^0_{ej} as:

$$R^0_{ej} = \left(\frac{M_{ej}}{4\pi\rho_0 \ln(x)}\right)^{1/3}. \tag{C.2.4}$$

In summary, the initial conditions are set once the values of E_0 and v_{ej} are given. Later, an approximate value of x is found numerically with equation C.2.1, R^0_{ej} is obtained with equation C.2.4 and R_c from equation C.2.2.

As an example of the procedure, let us determine the initial conditions fulfilling the data from Terlevich et al. (1992). They set $M_{ej} = 2.5$ $M_\odot$, and state that an initial energy $E = 10^{51}$ erg and momentum $p_0 = 2.44 \times 10^{42}$ g cm s^{-1} were deposited into an ambient medium of $n_0 = 10^7$ cm^{-3}.

There is a degeneracy on this prescription of the problem, due to the fact that several velocities v_{ej} can satisfy these conditions and also satisfy the equation C.2.1. In this case, $v_{ej} = 1.4 \times 10^4$ km s^{-1} is set and equation C.2.1 gives $x \approx 6.25$. The different parameters for this example are shown in Table C.1.

Table C.1: Initial conditions for a SNR evolving into a medium of density $n_0 = 10^7$ cm^{-3}.

M_{ej}[M$_\odot$]	2.5
v_{ej}[km s^{-1}]	1.4×10^4
E_0 [erg]	10^{51}
x	6.25
R^0_{ej}[10^{-2} pc]	0.70
R_c[10^{-2} pc]	0.11

Initial condition for the Thin-Shell code

Following the ideas from chapter 3, the Thin-Shell code is started under the supposition that a small fraction of the original kinetic energy has become thermal and kinetic energy of the shocked gas. Hence, this yields an initial time $t_0 > 0$. However, unlike chapter 3, this energy fraction will not be the starting point for the definition of the initial conditions.

The starting point is given by the initial position of the leading shock $R_{LS}(t_0)$:

$$R_{LS}(t_0) = R^0_{ej} + \alpha R^0_{ej}, \tag{C.3.1}$$

i.e., the leading shock is assumed to have travelled at a velocity $4/3 v_{ej}$ to a position that is off by $(1+\alpha)$ from the original position. In this equation, α will be adjusted iteratively (usually $\alpha < 0.15$). Equation C.3.1 in turn yields an initial time t_0:

$$t_0 = \frac{3/4 \alpha R^0_{ej}}{v_{ej}}. \tag{C.3.2}$$

As in chapter 3, the initial position of the reverse shock $R_{RS}(t_0)$ is set as:

$$R_{RS}(t_0) = R_{LS}(t_0)/l_{ED}, \tag{C.3.3}$$

with $l_{ED} \approx 1.1$. The initial velocity of the reverse shock is the maximum velocity of the ejecta at $R_{RS}(t_0)$:

$$V_{LS}(t_0) = \frac{R_{RS}(t_0) - R_c}{R_{LS}(t_0) - R_c} v_{ej} = V_{max}. \tag{C.3.4}$$

Equations C.3.3 and C.3.4 lead to the initial velocity of the leading shock $V_{LS}(t_0)$:

$$V_{LS}(t_0) = l_{ED} V_{RS}(t_0) = l_{ED} V_{max}. \tag{C.3.5}$$

The initial velocity of the shocked gas is:

$$U_{ini} = \frac{2}{\gamma + 1} l_{ED} V_{max}. \tag{C.3.6}$$

The equation of energy conservation at t_0 is:

$$E_0 = E^0_{k,ism} + E^0_{th} + E^0_{k,ej} + E^0_{k,free}. \tag{C.3.7}$$

The fraction of thermalized ejecta mass is non-zero at t_0 and therefore $E^0_{k,ej} > 0$. Similarly, the leading shock has already swept-up some of the ambient gas and hence $E^0_{k,ism} > 0$. Equation C.3.7 allows one to calculate E^0_{th}. The parameter α is adjusted iteratively until $E^0_{th} > 0$.

References

Apostol T., 2007, Calculus, Volume Ii, 2nd Ed Multi-variable Calculus and Linear Algebra, with Applications to Differential Equations and Probabil. No. v. 2 in Calculus, Wiley India Pvt. Limited, https://books.google.com.mx/books?id=mw92eOTozCcC

Bianchi S., Schneider R., 2007a, MNRAS, 378, 973

Bianchi S., Schneider R., 2007b, MNRAS, 378, 973

Bisnovatyi-Kogan G. S., Silich S. A., 1995, Reviews of Modern Physics, 67, 661

Blondin J. M., Wright E. B., Borkowski K. J., Reynolds S. P., 1998, ApJ, 500, 342

Borkowski K. J., Lyerly W. J., Reynolds S. P., 2001, ApJ, 548, 820

Chevalier R. A., 1977, ARA&A, 15, 175

Chevalier R. A., 1982a, ApJ, 258, 790

Chevalier R. A., 1982b, ApJ, 259, 302

Cioffi D. F., McKee C. F., Bertschinger E., 1988a, ApJ, 334, 252

Cioffi D. F., McKee C. F., Bertschinger E., 1988b, ApJ, 334, 252

Clarke C., Carswell B., 2007, Principles of Astrophysical Fluid Dynamics. Principles of Astrophysical Fluid Dynamics, Cambridge University Press, https://books.google.com.mx/books?id=odiiDgAAQBAJ

Conroy C., Spergel D. N., 2011, ApJ, 726, 36

Dormand J. R., Prince P. J., 1980, Journal of computational and applied mathematics, 6, 19

Draine B. T., McKee C. F., 1993, ARA&A, 31, 373

Dunne L., Eales S., Ivison R., Morgan H., Edmunds M., 2003, Nature, 424, 285

Elmegreen B. G., 2017, ApJ, 836, 80

Fabian A. C., Stewart G. C., Brinkmann W., 1983, in Danziger J., Gorenstein P., eds, IAU Symposium Vol. 101, Supernova Remnants and their X-ray Emission. pp 119–124

Franco J., Tenorio-Tagle G., Bodenheimer P., Rozyczka M., 1991, PASP, 103, 803

Gaffet B., 1978, ApJ, 225, 442

Gull S. F., 1973, MNRAS, 161, 47

Gull S. F., 1975, MNRAS, 171, 263

Haid S., Walch S., Naab T., Seifried D., Mackey J., Gatto A., 2016, MNRAS, 460, 2962

Hamilton A. J. S., Sarazin C. L., 1984, ApJ, 281, 682

Hines D. C., Krause O., Rieke G. H., Fan X., Blaylock M., Neugebauer G., 2006, ApJ, 641, L85

Hnatyk B., Petruk O., 1999, A&A, 344, 295

Hwang U., Laming J. M., 2012, ApJ, 746, 130

Kim C.-G., Ostriker E. C., 2015, ApJ, 802, 99

Krause M., Charbonnel C., Decressin T., Meynet G., Prantzos N., 2013, A&A, 552, A121

Laming J. M., Hwang U., 2003, ApJ, 597, 347

LeVeque R., Steiner O., Gautschy A., Mihalas D., Dorfi E., Müller E., 2006, Computational Methods for Astrophysical Fluid Flow: Saas-Fee Advanced Course 27. Lecture Notes 1997 Swiss Society for Astrophysics and Astronomy. Saas-Fee Advanced Course, Springer Berlin Heidelberg, https://books.google.com.mx/books?id=xOYFCAAAQBAJ

Li M., Ostriker J. P., Cen R., Bryan G. L., Naab T., 2015, ApJ, 814, 4

Maiolino R., Schneider R., Oliva E., Bianchi S., Ferrara A., Mannucci F., Pedani M., Roca Sogorb M., 2004, Nature, 431, 533

Marchenko S. V., 2006, in Lamers H. J. G. L. M., Langer N., Nugis T., Annuk K., eds, Astronomical Society of the Pacific Conference Series Vol. 353, Stellar Evolution at Low Metallicity: Mass Loss, Explosions, Cosmology. p. 299 (arXiv:astro-ph/0511147)

Martínez-González S., Tenorio-Tagle G., Silich S., 2016, ApJ, 816, 39

McKee C. F., Ostriker J. P., 1977, ApJ, 218, 148

McKee C. F., Truelove J. K., 1995, Phys. Rep., 256, 157

Micelotta E. R., Dwek E., Slavin J. D., 2016, A&A, 590, A65

Mihalas D., Mihalas B., 2013, Foundations of Radiation Hydrodynamics. Dover Books on Physics, Dover Publications, https://books.google.com.mx/books?id=GVK8AQAAQBAJ

Morgan H. L., Dunne L., Eales S. A., Ivison R. J., Edmunds M. G., 2003, ApJ, 597, L33

Nozawa T., Kozasa T., Tominaga N., Maeda K., Umeda H., Nomoto K., Krause O., 2010, ApJ, 713, 356

Orlando S., Miceli M., Pumo M. L., Bocchino F., 2016, ApJ, 822, 22

Ostriker J. P., McKee C. F., 1988, Reviews of Modern Physics, 60, 1

Petruk O., 2006, ArXiv Astrophysics e-prints,

Press W., 2007, Numerical Recipes 3rd Edition: The Art of Scientific Computing. Cambridge University Press, https://books.google.com.mx/books?id=1aAOdzK3FegC

Raymond J. C., Cox D. P., Smith B. W., 1976, ApJ, 204, 290

Rodríguez-González A., 2000, Master's thesis, Instituto Nacional de Astrofísica, Óptica y Electrónica, Puebla, México

Schure K. M., Kosenko D., Kaastra J. S., Keppens R., Vink J., 2009, A&A, 508, 751

Sedov L. I., 1946, Dokl. Akad. Nauk SSSR, 42, 17

Silich S. A., 1992, Ap&SS, 195, 317

Silich S., Tenorio-Tagle G., 2017, MNRAS, 465, 1375

Silich S., Tenorio-Tagle G., 2018, MNRAS, 478, 5112

Slane P., Chen Y., Schulz N. S., Seward F. D., Hughes J. P., Gaensler B. M., 2000, ApJ, 533, L29

Tang X., Chevalier R. A., 2017, MNRAS, 465, 3793

Tenorio-Tagle G., 1996, AJ, 111, 1641

Tenorio-Tagle G., Bodenheimer P., Franco J., Rozyczka M., 1990, MNRAS, 244, 563

Tenorio-Tagle G., Rozyczka M., Franco J., Bodenheimer P., 1991, MNRAS, 251, 318

Tenorio-Tagle G., Silich S., Martínez-González S., Muñoz-Tuñón C., Palouš J., Wünsch R., 2013, ApJ, 778, 159

Tenorio-Tagle G., Muñoz-Tuñón C., Silich S., Cassisi S., 2015, ApJ, 814, L8

Terlevich R., Tenorio-Tagle G., Franco J., Melnick J., 1992, MNRAS, 255, 713

Thornton K., Gaudlitz M., Janka H.-T., Steinmetz M., 1998, ApJ, 500, 95

Todini P., Ferrara A., 2001, MNRAS, 325, 726

Truelove J. K., McKee C. F., 1999, ApJ, 120, 299

Wiersma R. P. C., Schaye J., Smith B. D., 2009, MNRAS, 393, 99

Zel'dovich Y., Raizer Y., 2012, Physics of Shock Waves and High-Temperature Hydrodynamic Phenomena. Dover Books on Physics, Dover Publications, https://books.google.com.mx/books?id=PULCAgAAQBAJ